2014

Modified Seed Growth of Iron Oxide Nanoparticles in Benzyl Alcohol: Magnetic Nanoparticles for Radio Frequency Hyperthermia Treatment of Cancer

Stanley E. Gilliland III
Virginia Commonwealth University, gillilandse@mymail.vcu.edu

Modified Seed Growth of Iron Oxide Nanoparticles in Benzyl Alcohol: Magnetic Nanoparticles for Radio Frequency Hyperthermia Treatment of Cancer

A thesis submitted in partial fulfillment of the requirements for the degree of Master of Science at Virginia Commonwealth University.

By
Stanley Eugene Gilliland III
Bachelor of Science
James Madison University
December 2010

Director: Dr. Everett E. Carpenter
Professor, Department of Chemistry
Co-Director: Dr. Michael D. Shultz
Research Biologist - McGuire VA Medical Center
& Adjunct Faculty, Department of Chemistry

Virginia Commonwealth University
Richmond, Virginia
December 2014

Acknowledgment

Over the past several years I have come to know many people that are highly deserving of thanks for helping or supporting the writing of this thesis. My beautiful and loving wife Ruthie has always given her unwavering love, and continual support. Our beautiful baby girl Emily is always ready with a smile or a laugh to rejuvenate my spirit. When the stress accumulated or the research did not go as expected I only had to close my eyes and imagine their faces to feel their love and encouragement. I would like to thank my mom, dad, brother, sister, and other family members who were always there to give their honest opinion and advice, push me to achieve higher goals, and believe in me even when I did not.

Dr. Carpenter deserves appreciation for advising my research and going out of his way to ensure that I am equipped with the knowledge I need to succeed. My co-advisor Dr. Shultz has always been there to inspire and try new ideas. Thank you for constantly pushing me to think independently and come up with new ideas. My deepest appreciation goes out to my committee members and the VCU Chemistry Department for the opportunity to study and research chemistry. I would also like to thank my lab mates from across town that are always helpful, willing to teach me an experimental technique, and keep me in the loop. I especially want to thank the VCU Nanomaterials Core Characterization Facility for instrument access and Dustin Clifford for help with TEM imaging.

Table of Contents

List of Tables

Chapter 2.

Chapter 3.

List of Figures

Chapter 2.

Chapter 3.

List of Abbreviations and Symbols

$\left(\frac{\Delta T}{\Delta t}\right)$ -	Initial linear temperature increase per unit time
⟨Γ ⟩-	average decay rate
1/T-	Effective relaxation time
A-	Amperes
AC-	Alternating Current
b-	Full Width Half Maximum (FWHM)
c_{H2O}-	Specific heat capacity of water
c_{np}-	Specific heat capacity of nanoparticles
CVD-	Chemical Vapor Deposition
D_f-	Diffusion coefficient
d_{hkl}-	distance between atomic planes of lattice
DLS-	Dynamic Light Scattering
E_A-	Energy Barrier
EPR-	Enhanced Permeation and Retention
f-	frequency
FCC-	Face Centered Cubic
$Fe(acac)_3$-	Iron (III) acetylacetonate
$FeCl_2$-	Iron (II) Chloride
g-	gram
H-	Magnetic field strength
H_C-	Coercivity
I-	Current
ILP-	Intrinsic Loss of Power
K-	Magnetocrystalline anisotropy constant
K-	Shape factor
K_B-	Boltzmann constant
k_BT-	Thermal energy
L-	Length of a coil
M-	Magnetization
MCL_{hkl}-	Coherently scattering domain that is perpendicular to the hkl plane
MFH-	Magnetic Fluid Hyperthermia
m_{H2O}-	mass of water
m_{np}-	mass of nanoparticles
M_R-	Remnant Magnetization
MRI-	Magnetic Resonance Imaging
M_S-	Magnetization Saturation
n-	Integer
N-	Number of turns in a coil

n-	refractive index
N_2-	Nitrogen
NaCl-	Sodium Chloride
NaOH-	Sodium Hydroxide
O-	Oxygen
OH-	Hydroxide
PDI-	Polydispersity index
q-	magnitude of scattering wave
RF-	Radiofrequency
R_H-	Hydrodynamic radius
SAR-	Specific Absorption Rate
T-	Temperature
T_B-	Brownian relaxation time
TEM-	Transmission Electron Microscopy
TGA-	Thermogravimetric analysis
T_M-	Morin Temperature
T_N-	Néel relaxation time
T_N-	Néel Temperature
V_C-	Volume of the core particle
V_H-	Hydrodynamic Volume
VSM-	Vibrating Sample Magnetometery
W-	Watt
X-	Magnetic Susceptibility
XRD-	X-ray Diffraction
η-	Viscosity
θ -	Incident Angle
θ **DLS**-	Range of scattering angle
λ -	Wavelength
μ_2-	Variance of the decay rate distribution
μ_B-	Bohr magneton
μ_o-	Permeability of free space
$\tau_o E_A$-	pre-exponential factor

Abstract

MODIFIED SEED GROWTH OF IRON OXIDE NANOPARTICLES IN BENZYL ALCOHOL: MAGNETIC NANOPARTICLES FOR RADIO FREQUENCY HYPERTHERMIA TREATMENT OF CANCER

By Stanley Eugene Gilliland III, B.S.

A thesis submitted in partial fulfillment of the requirements for the degree of Master of Science at Virginia Commonwealth University.

Virginia Commonwealth University, 2014.

Major Director: Dr. Sarah Rutan, Professor,
Director of Graduate Studies,
Department of Chemistry
Research Director: Dr. Everett E. Carpenter
Professor, Department of Chemistry
Research Co-Director: Dr. Michael D. Shultz
Research Biologist - McGuire VA Medical Center
& Adjunct Faculty, Department of Chemistry

Iron oxide nanoparticles have received sustained interest for biomedical applications as synthetic approaches are continually developed for precise control of nanoparticle properties. This thesis presents an investigation of parameters in the benzyl alcohol synthesis of iron oxide nanoparticles. A modified seed growth method was designed for obtaining optimal nanoparticle properties for magnetic fluid hyperthermia. With a one or two addition process, iron oxide nanoparticles were produced with crystallite sizes ranging from 5-20 nm using only benzyl alcohol and iron

precursor. The effects of reaction environment, temperature, concentration, and modified seed growth parameters were investigated to obtain precise control over properties affecting radiofrequency heat generation. The reaction A2-24(205)_B2-24(205) produced monodispersed (PDI=0.265) nanoparticles with a crystallite size of 19.5±1.06 nm and the highest radiofrequency heating rate of 4.48$\frac{\left(\frac{^{\circ}C}{min}\right)}{mg}$ (SAR=1,175.56$\frac{W}{g}$, ILP=3.1127$\frac{nHm^2}{kg}$) for the reactions investigated. The benzyl alcohol modified seed growth method offers great potential for synthesizing iron oxide nanoparticles for radiofrequency hyperthermia.

Chapter 1: Introduction and Background

1.1 Radiofrequency Induced Hyperthermia: Treatment of Cancer

In 1957 Gilchrist first reported the idea of using magnetic particles for hyperthermia treatment of tumors.[1] Hyperthermia is often divided into three temperature ranges that have various effects and interactions with other therapies.[2,3] Mild hyperthermia (39-42°C) is considered non-lethal temperature elevation and has been shown to sensitize tumors to chemotherapy or radiation by increased drug perfusion and oxygenation.[3-5] Moderate hyperthermia (41-46°C) causes cells to experience heat stress, promotes protein degradation and interrupts vital cellular processes eventually leading to apoptosis.[6-8] Thermoablation (>45°C) generates enough heat to directly destroy local tumor cells and tissues via necrosis, carbonization, and coagulation.[6,8-11] While there is no direct heat sensitivity of tumor cells compared to normal tissue, cancerous tumors have regions of hypoxia and low pH due to the chaotic vasculature of tumors.[12,13] This allows for selective cell killing of tumors when hyperthermia is in the range of 40-44°C.[12] In order to produce these heating effects in tumors by magnetic particles, an external radiofrequency (RF) alternating current (AC) magnetic field is applied which heats magnetic particles by eddy currents, dielectric losses, or hysteretic

heating.[1] The extent and rate of particle heating depends on the size, conductivity and magnetic properties of the material.[1,2,14-17] Gilchrist found that the frequency and field strength applied must be optimized to provide minimal heating of healthy tissue due to dielectric loss and maximize hysteretic heating of the magnetic particles.[1] In this regard, frequencies below 100 MHz have high RF penetration and low RF absorption in human tissue for magnetic resonance imaging (MRI).[18] It is highly desirable that high heating rates are achieved for the lowest possible frequencies and/or magnetic field strengths.[19] It was determined that for safe magnetic hyperthermia the magnetic field strength and frequency product (H×f) should be lower than $5\times10^9 \frac{A}{ms}$ when heating a human torso for 1 hour.[19] High H×f values will produce more unwanted and nonspecific heating of both cancerous and healthy tissue due to eddy currents.[19] This value was can be exceeded for smaller tissue areas and depending on the location of the cancer and health of the patient.[19] The RF coil used in this work has an H×f value of $1.01\text{x}10^{10} \frac{A}{ms}$, which is at an acceptable level for *in vitro* studies and *in vivo* studies in small animals.[20] Utilizing higher frequencies and magnetic field strengths, larger SAR values can be obtained. However, the time allowed for heating must decrease for these higher f and H values to deliver safe heating without discomfort to the patient. Therefore, the RF heating tests were conducted for 10 minutes instead of 1 hour. It has been shown that for "Micromods nanomag 100 nm" nanoparticles the SAR has a linear relationship with RF coil frequencies between 100-900 kHz.[21]

1.2 Switching to Nanoparticles: Néel and Brownian Relaxation Mechanisms

Research in magnetic particle based hyperthermia has shifted from larger multi-domain particles, similar to Gilchrist's research, to smaller single-domain and superparamagnetic materials. The primary reason for this shift is that superparamagnetic nanoparticles are much more efficient at absorbing power to generate heat than microparticles.[2] Superparamagnetic nanoparticles generate heat by two mechanisms. The Néel relaxation mechanism generates heat through quickly altering the direction of magnetic moments with respect to the crystal lattice.[6] In other words, the alternating current (AC) magnetic field applied provides the necessary energy for the dipole to overcome an energy barrier, due to the particle volume and magnetocrystalline anisotropy, and internally alter directions.[22,23] The equation for the energy barrier (E_A) is shown in **Equation 1a**. For iron oxide with a crystallite diameter less than 8 nm, the Néel relaxation mechanism is determined by the pre-exponential term.[23] Between 8 nm and 15 nm, the Néel relaxation mechanism is determined by the exponential term until Brownian relaxation mechanism becomes dominant (>16 nm).[23] The Brownian mechanism generates heat as a result of viscosity of the media resisting the physical rotation of the nanoparticles in an applied AC magnetic field thus releasing mechanical energy and heating the surrounding media.[22,24] The internal, Néel, and external, Brownian, sources of friction generate heat by loss of thermal and mechanical energy.[22,24] The equations for Néel relaxation time (τ_N)[25] and Brownian relaxation time (τ_B)[25-27] are shown in **Equation 1b and c**.[14,28-30] K is the magnetocrystalline anisotropy constant, V_c is volume of the core particle, $\tau_o E_A$ is the pre-exponential factor, V_h is hydrodynamic volume of the particle, T is temperature, k_B is Boltzmann constant, and η is medium viscosity. The effective relaxation time ($1/\tau$), shown in **Equation 1d**,

describes the combined relaxation mechanisms and is dominated by the relaxation mechanism with a shorter relaxation time.[25] The Néel heating mechanism dominates at small particle sizes and Brownian mechanism takes over at larger particle sizes.[14,15,22,30-32]

$$E_A = \mathrm{K}\mathrm{V}_c \tag{1a}$$

$$\tau_N = \tau_o \mathrm{E}_A \exp\left(\frac{\mathrm{E}_A}{k_B \mathrm{T}}\right) \tag{1b}$$

$$\tau_B = \frac{3\eta \mathrm{V}_h}{k_B \mathrm{T}} \tag{1c}$$

$$\frac{1}{\tau} = \frac{1}{\tau_N} + \frac{1}{\tau_B} \tag{1d}$$

Several factors therefore can affect which mechanism of heating dominates, such as size, polydispersity, crystal structure, shape, and magnetocrystalline anisotropy.[22,24] Wide polydispersity particle solutions can affect the effective heating due to the presence of small and large particles that generate heat by Néel and Brownian mechanisms respectively.[22]

In 1993 Jordan et al. used specific absorption rate (SAR) values to evaluate various parameters effects on hyperthermia efficiency.[14] However, this method of determining SAR is dependent on the equipment used or more specifically the magnetic field strength and frequency.[21,33] Also, the SAR values calculated in this fashion are often misused or misinterpreted when used to indicate heating capabilities of magnetic nanoparticles.[21] Heating capabilities can now be expressed in terms of intrinsic loss of power (ILP) which normalizes the SAR values by incorporating magnetic field strength and frequency of the heating equipment used to better compare the materials heating capability.[21,33-34] The equations for SAR and effective SAR are shown in **Equations 2a, and 2b** and ILP in **Equation 2c**. Where c_{H_2O} and c_{np} are the specific heat capacity of

water or nanoparticles $\left(\frac{\mathrm{W}\times s}{\mathrm{g}\times\mathrm{K}}\right)$, m_{np} is the mass of total nanoparticles, m_{H_2O} is the mass of water, $\left(\frac{\Delta T}{\Delta t}\right)$ is the initial linear temperature increase per unit time $\left(\frac{\mathrm{K}}{\mathrm{s}}\right)$, H is magnetic field strength applied $\left(\frac{\mathrm{A}}{\mathrm{m}}\right)$ and f is the AC magnetic field frequency (kHz).[30-32,34]

$$SAR = \frac{c}{m_{np}}\left(\frac{\Delta T}{\Delta t}\right) \quad (2a)$$

$$Effective\ SAR = \frac{c_{H_2O}m_{H_2O}+c_{np}m_{np}}{m_{np}}\left(\frac{\Delta T}{\Delta t}\right)\left(\frac{1}{H^2_{applied}\times f}\right) \quad (2b)$$

$$ILP = \frac{SAR}{H^2_{applied}\times f} \quad (2c)$$

It has been determined that the average crystallite size and narrow size distribution are two of the most important factors in maximizing energy absorption and heat production.[17,35]

Other reasons for shifting to nanoparticles are that larger particles tend to be more invasive, have a higher potential for adverse damage to surrounding healthy cells, and do not generate uniform heating.[2] Also, unlike larger magnetic particles, superparamagnetic nanoparticles do not retain their magnetism after removal of an external magnetic field and are thus less likely to aggregate which prolongs blood circulation time.[36] Furthermore, with the combination of modern medicine and nanotechnology, nanoparticles can be specifically targeted to cancer cells to provide minimal invasiveness, and more local and confined heating.[2,6,17,37,38] For these reasons, synthesizing nanoparticles with high SAR values are of paramount importance and are rigorously investigated to improve hyperthermia treatment of cancer. Higher SAR values are needed to lower the concentrations of nanoparticles in tumors required to deliver effective hyperthermia therapy.[19,39] However, there have been several investigations that demonstrate reduced cell viability without measurable increases in macroscopic

temperature.[22,40,41] This would suggest that SAR or ILP values may not be indicative of effectiveness in hyperthermia cancer therapy.[22] Improvements need to be made for iron oxide nanoparticle hyperthermia to become clinically relevant. This includes, increasing SAR/ILP values, blood retention and tumor uptake, and decreasing toxicity and immunogenicity, while maintaining biocompatibility.[20,22] This can be accomplished by utilizing biocompatible materials in synthesis and surface functionalization.

1.3 Iron Oxide for Magnetic Hyperthermia: Ideal Properties and Challenges to Overcome

More specifically, iron oxide nanoparticles are a primary candidate for nanomedicine therapeutic applications in part due to their RF induction heating properties, as well as being biocompatible and biodegradable.[22,35,36,42] The body metabolizes the iron ions and will be used to form hemoglobin by erythrocytes.[43] In addition, they can be classified as a theranostic agent[44-47] providing diagnostic imaging capabilities in the form of a MRI contrast[48,49] and therapeutic potential by means of Magnetic Fluid Hyperthermia (MFH).[35,49,50] The US FDA has approved iron oxide for use in iron supplements[51-53] and for MRI in the liver.[54] Superparamagnetic iron oxide nanoparticles coated with aminosilanes are also currently in clinical trials in Germany for MFH treatment of glioblastoma and prostate cancer.[37,50,55]

The optimal iron oxide nanoparticles, for heat generation by RF induction heating, have been shown to have a crystallite size of 15-16 nanometers (nm).[30,56] This size gives the ideal combination of heating mechanisms, with Néel relaxation being the dominant process.[10] Above this size, Brownian relaxation becomes the dominant

heating mechanism which typically yields lower heat generation.[10] Although hyperthermia can be delivered regionally or to the whole body through the use of thermoseeds, water bath, ultrasound, microwave, or infrared radiation, there is still a demand for a therapy that can deliver sufficient hyperthermia to smaller target areas with less invasive procedures.[22,57] Iron oxide nanoparticles offer the potential to generate sufficient heating to localized tumors with minimal invasiveness and have the advantage of intracellular localization either through tumor selective enhanced permeation and retention (EPR) or targeting strategies.[22,58]

The main challenge to overcome is to develop an iron oxide synthesis that produces iron oxide nanoparticles that are easily surface functionalized for biostability and targeting for increased tumor uptake.[22] Thus, optimization and investigation of iron oxide nanoparticle synthesis to control and obtain the best combination of crystallite size, particle size, monodispersity and magnetic properties, while maintaining minimal toxicity and ease of surface functionalization is of continually growing interest.

1.4 Methods of Synthesizing Iron Oxides

Iron oxide nanoparticles can be synthesized by various methods such as electron beam lithography[59], mechanical alloying or ball milling[60-63], electrospray[64], laser pyrolysis[65-69], or gas-phase deposition[70].[49] However, some of these methods are complex and/or lack adequate size control on the nano scale. Alternatively, iron oxide nanoparticles can also be produced by synthetic strategies including sol-gel[71], aqueous co-precipitation[72-77], hydrothermal reaction[78], microemulsion[79], flow injection synthesis[80], chemical vapor deposition (CVD)[81,82],thermal decomposition[83-86], glycol[48,87-89], and

sonochemical synthesis[90].[23,91,92] Co-precipitation of iron salts is the most widely used method for synthesizing iron oxide nanoparticles because it can produce large quantities of iron oxide nanoparticles easily, but this method lacks adequate control over size distribution.[23,93]

Thermal decomposition synthesis of iron oxide is a very versatile method that allows for the control of morphology and size.[23] Control is obtained by varying reaction time, temperature, reactants concentration and/or ratio, inherent properties of the solvent and iron precursor, and through the use of seed growth methods.[23,94] The use of non-polar solvents allows for tunable size, high crystallinity, easy scale-up, and a narrow size distribution of nanoparticles, but they can be more difficult to phase transfer, functionalize and purify for biological applications. In addition, most of these approaches rely on several seed growth steps with intermediate wash steps, multiple solvents and capping agents to obtain the desired 15 nm crystallite size for iron oxide nanoparticles.[84,95] The synthesized nanoparticles then undergo rigorous phase transfer processes and functionalizing methods to produce a biologically stable colloidal suspension. MFH and nanomedicine in general rely heavily on maintaining biological stability of the nanoparticles and the ability to carry targeting ligands to increase the affinity to tumor cells.[37,38,96] Thus, synthesizing nanoparticles that are easily functionalized, purified, stable in various media, and can be further functionalized with targeting or therapeutic modalities is of paramount importance.

1.5 Benzyl Alcohol Synthesis of Metal Oxides

Benzyl alcohol will be used as the solvent, capping agent and reducing agent for the combined reduction and thermal decomposition of iron (III) acetylacetonate ($Fe(acac)_3$). Benzyl alcohol is a polar solvent and allows for the control of size, high crystallinity, easy scale-up, narrow size distribution, and facile surface coating for biological stability after thermal decomposition synthesis.[97] Benzyl alcohol is found naturally in oils of plants and used in cosmetic products,[98] as a flavor and fragrance additive,[98-100] and as a preservative of injectable drugs.[101] Benzyl alcohol has been used as the solvent to synthesize highly crystalline titania nanoparticles from titanium tetrachloride with control over the size by simply adjusting temperature and precursor concentrations.[102] Other transition metal chlorides were used in benzyl alcohol synthesis to create vanadium and tungsten oxide and can be scaled up to produce gram amounts of product.[103] Benzyl alcohol can be used to synthesize 35 different metal oxides from metal precursors including metal acetylacetonates, alkoxides, acetates and halides.[104-109] While benzyl alcohol has been used as the solvent in many metal oxide syntheses, relatively few have been done with $Fe(acac)_3$.[104,105] Microwave mediated benzyl alcohol synthesis using $Fe(acac)_3$ as the metal precursor led to high crystallinity iron oxide nanoparticles in a few minutes, but with crystallite sizes of only 5 nm.[105] While quick reaction time offers a substantial benefit, this method may not have sufficient control over crystallite sizes in the range applicable to magnetic hyperthermia. Autoclave mediated benzyl alcohol synthesis using $Fe(acac)_3$ as the metal precursor was able to produce crystallites ranging from 15-25 nm, however this required the use of a glovebox, autoclave and furnace heating at 175°C or 200°C for two days.[109] The

complicated set-up for this synthesis hinders its applicability. By utilizing the benzyl alcohol synthesis under nitrogen and atmospheric conditions it may be possible to discern mechanistic insight into reaction with $Fe(acac)_3$ and gain better control over crystallite size and polydispersity, which are the most vital material properties in increasing heat generation in radiofrequency hyperthermia.

1.6 Project Overview

The overall objective of this thesis was to better understand and improve the benzyl alcohol approach to synthesize iron oxide nanoparticles specifically for radiofrequency induced magnetic hyperthermia applications. In Chapter 1, an introduction and relevant background information to iron oxide nanoparticles for radiofrequency induced magnetic hyperthermia was presented.

Chapter 2 presents a more detailed description of iron oxide nanoparticles. Iron oxides have 16 known crystallite structures with numerous applications in nanotechnology. The crystal structure and magnetic properties of several of the iron oxides are reviewed, with emphasis on magnetite and maghemite which are commonly used in magnetic hyperthermia.

Chapter 3 presents the benzyl alcohol synthesis of iron oxide and the investigation of synthetic parameters on the resultant nanoparticle characteristics. The effects of reaction environment, time, temperature and concentration were investigated to gain insight into the mechanism of benzyl alcohol synthesis. The results were rationalized using LaMer growth and Ostwald ripening principles. A modified seed growth procedure was designed and applied to the benzyl alcohol method for further

optimization and control of iron oxide properties important in radiofrequency induced magnetic heating. The complex relationships between iron oxide nanoparticle characteristics and radiofrequency heating are discussed.

Knowledge gained from designing and optimizing a synthesis of iron oxide nanoparticles specifically for the application of magnetic hyperthermia therapy for cancer will be widely beneficial. Understanding how different parameters affect the nucleation, growth, and nanoparticle properties will be of considerable interest to natural product chemists, physical chemists, synthetic chemists, molecular biologists, biochemists, and physicists.

Chapter 2: Iron Oxide Nanoparticles

2.1 Iron Oxides in Nanotechnology

Magnetic nanomaterials, such as iron oxide, have numerous potential applications. Some of these include high-density information data storage,[110-113] ferrofluids,[114] magnetic sensors,[115-118] catalysts,[110,119-122] and permanent magnets.[112,113,123,124] Magnetic information data storage relies on controlling the magnetocrystalline anisotropy of iron oxide to provide unique ways of storing data.[111] Permanent magnet applications combine the properties of magnetically "hard" (high magnetization saturation) and "soft" (large coercivity) materials by exchange coupling to produce a magnet with high saturation magnetization and large coercivity values.[113] Catalysts and magnetic sensors benefit from the use of iron oxide nanoparticles because of their high surface area to volume ratio enabling them to be more efficient, stable and selective than their bulk counterparts.[120] An advantage over other nanoparticles for catalysis and sensing applications is their inherent magnetism allowing them to be magnetically recoverable and isolatable.[120] Biotechnology and nanomedicine utilize iron oxide nanoparticles for diagnostic and therapeutic applications. Iron oxide

nanoparticles as MRI contrast agents have been widely researched and show strong T2-weighted and T2* image enhancement.[25,125-129] Iron oxide nanomaterials are also being researched and clinically tested for use as drug delivery and magnetic hyperthermia applications due to their small size, biocompatibility, surface functionalizability, and imaging capabilities.[30,42,125,130-132]

2.2 Iron Oxide Crystal Structures

Iron oxides can be commonly found in the environment usually in the form of iron(II) or iron (III) cations or some combination of the two cations.[92,133,134] The iron cations can form crystal structures with O_2^- and/or OH^- anions, and are termed oxides, hydroxides, or oxide-hydroxides. However, iron oxide is a general term that often refers to the oxides, hydroxides and oxide-hydroxides.[92] There are currently sixteen known iron oxides pure phases with differing stoichiometry and crystal structures.[92,133,135] The iron oxides can be subcategorized as iron oxide, iron hydroxide, and iron oxide-hydroxides and are shown in **Table 2.1**.[135] The crystal structures of magnetite, maghemite, hematite, and wüstite are briefly discussed in the following sections.

Table 2.1. The sixteen known pure phase iron oxides categorized into iron oxide, iron hydroxide and iron oxide-hydroxide. Reproduced from[135].

Iron Oxide	
Mineral Name	**Formula**
Wüstite	FeO
Magnetite	Fe_3O_4
Hematite	α-Fe_2O_3
β-Maghemite	β-Fe_2O_3
Maghemite	γ-Fe_2O_3
ε-maghemite	ε-Fe_2O_3
High pressure iron oxide	Fe_4O_5
Iron Hydroxide	
Mineral Name	**Formula**
Iron(II) hydroxide	$Fe(OH)_2$
Bernalite (Iron(III) hydroxide)	$Fe(OH)_3$
Iron Oxide-Hydroxide	
Mineral Name	**Formula**
Goethite	α-FeOOH
Akaganéite	β-FeOOH
Lepidocrocite	γ-FeOOH
Feroxyhyte	δ-FeOOH
High Pressure FeOOH	FeOOH
Ferrihydrite	$Fe_5HO_8 \cdot 4H_2O$ approx.
Schwertmannite	$Fe_{16}O_{16}(OH)_y(SO_4)_z \cdot nH_2O$
Green Rusts	$Fe_x^{3+}Fe_y^{2+}(OH)_{3x+2y-z}(A^-)_z$; $A^- = Cl^-, 1/2SO_4^{2-}, CO3^{2-}$

2.2.1 Magnetite Crystal Structure

The crystal structure of magnetite is an inverse spinel structure.[25,110,135-138] as represented in **Figure 2.1.**[139] In this structure, 32 oxygen atoms are arranged in a close packed face centered cubic (FCC) array with iron atoms occupying 1/8 of the 64 tetrahedral and ½ of the 32 octahedral vacancies.[25,135,136] Properties of magnetite are

shown in **Table 2.2.** reproduced from [135]. The Fe_3O_4 formula can be written as $Fe^{3+}(Fe^{2+}Fe^{3+})O_4$ to indicate the inverse spinel structure where eight Fe^{3+} ions occupy the tetrahedral sites and an equal mixture of sixteen Fe^{2+} and Fe^{3+} ions occupy the octahedral sites.[25,136,138] The tetrahedral and octahedral sites can be considered as sublattices within the FCC lattice of oxygen atoms. The iron ions in both the octahedral and tetrahedral sublattices are coupled ferrimagnetically.[136,138] Hund's rule indicates that the magnetic moments of Fe^{3+} and Fe^{2+} ions contain 5 Bohr magnetons (μ_B) and $4\mu_B$, respectively.[136] The eight Fe^{3+} ions in the octahedral and the eight Fe^{3+} ions in the tetrahedral sites are coupled antiferromagnetically and essentially cancel each other out so that only the Fe^{2+} ions contribute to the magnetization to give magnetite a calculated μ_B=4.07 per formula unit closer to that expected of Fe^{2+} ions.[136,137] Thus, the iron ions in the two sublattices are arranged ferrimagnetically with respect to each other.[136] Unequal amounts of Fe^{2+} and Fe^{3+} ions and the difference in Bohr magnetons between the two iron ions give rise to a net magnetic moment that couples ferrimagnetically.[136]

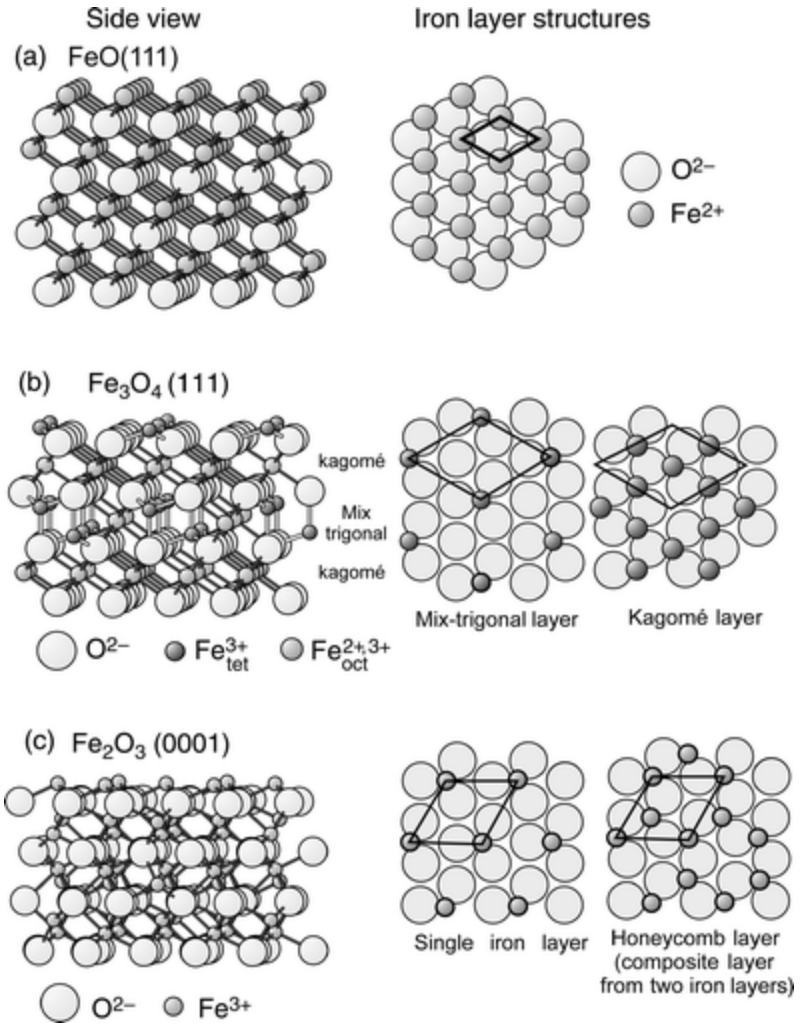

Figure 2.1. Diagram showing the side view and top view of wüstite (a), magnetite (b), and hematite(c). Two top views are shown for magnetite and hematite to visualize the different layers of the crystal structure. From [139]

Table 2.2. Properties of magnetite, maghemite, hematite and wüstite. Reproduced from [135].

Mineral Name	Magnetite	Maghemite	Hematite	Wüstite
	Cubic	Cubic or tetragonal	Rhombohedral hexagonal	Cubic
Cell Dimensions (nm)	a= 0.8396	a= 0.83474	a= 0.50356 c= 1.37489	a= 0.4302-0.4275
Formula units, per unit cell, Z	8	8	6	4
Density (g/cm^3)	5.18	4.87	5.26	5.9-5.99
Octahedral occupancy	-	-	2/3	-
Color	Black	Reddish-brown	Red	Black
Hardness	5.5	5	6.5	5
Magnetism	Ferrimagnetic	Ferrimagnetic	Weekly ferromagnetic or antiferromagnetic	Antiferromagnetic
Currie (Néel) Temperature (K)	850	820-986	956	203-211[1)]
Melting point (°C)	1583-1597		1350	1377
Boiling point (°C)	2623			2512

1) Néel Temperature

2.2.2 Maghemite Crystal Structure

The crystal structure of maghemite is an inverse spinel structure and closely related to the structure of magnetite. [110,135,139-141] The difference is due to the fact that most of the Fe ions are Fe^{3+}.[135] It consists of 32 oxygens, 21 1/3 Fe^{3+} and 2 1/3 vacancies in the octahedral sites.[135,140,141] Properties of maghemite are shown in **Table 2.2.** reproduced from [135]. Maghemite has a reddish-brown color and is a ferrimagnet.[141,142] γ-Fe_2O_3 is metastable and closely resembles the structure of Fe_3O_4.[110,138,141] At high temperatures the metastable maghemite is converted to

hematite.[141] The temperature at which this occurs depends on the size and crystallinity, however it has been reported to generally occur at 400°C.[135] Magnetite can be oxidized to maghemite when heated in the presence of organic compounds.[141,142] When this occurs, the Fe^{2+} ions in the octahedral sites of magnetite are oxidized to Fe^{3+} ions and leave cation vacancies (X), thus the formula for maghemite can be written as $(Fe^{3+})_8(Fe^{3+}_{5/3}X_{2/3})_8O_{32}$.[138,141,142]

2.2.3 Hematite Crystal Structure

Hematite (α-Fe_2O_3) is the most common iron oxide found in nature.[110,141] It has a red color and is considered a ferromagnetic material.[110,135,142] The crystal structure (**Figure 2.1**) is closely related to rhombohedral corundum.[135,139] In the crystalline structure the oxygens are in a hexagonal close packed structure with Fe^{3+} ions in two-thirds of the octahedral sites.[110,135] Properties of hematite are shown in **Table 2.2.** reproduced from [135]. The structure of hematite is comprised of rhombohedrally centered hexagonal cells.[135,141] Below the Morin Temperature (T_M), 260 K, hematite is antiferromagnetic.[141]Hematite transitions to a paramagnetic state above the Néel Temperature (T_N) of 950 K.[141] In between the T_M and T_N, the spins are slightly canted, about 5°, resulting in a weak ferromagnetic state.[141] Magnetite, maghemite, and other iron oxides can be eventually oxidized under the correct conditions to hematite because hematite is the thermodynamically favored state.[141,142]

2.2.4 Wüstite Crystal Structure

The crystal structure of wüstite (**Figure 2.1**) resembles the crystal structure of sodium chloride (NaCl).[135] In this crystallite structure the oxygen anions are in a closed packed FCC arrangement and the Fe^{2+} ions reside in the octahedral interstitial sites.[135] Properties of wüstite are shown in **Table 2.2.** reproduced from [135]. This crystal structure can only be formed above 843K and is unstable and will revert to Fe and Fe_3O_4 below this temperature.[135] Depending on the partial pressure of oxygen and the temperature the Fe^{2+} ions are oxidized to Fe^{3+} ions resulting in 5-15% differences observed in the stoichiometry, $Fe_{1-x}O$.[138,143]

2.3 Magnetic Properties of Iron Oxide

The iron oxides commonly used in magnetic hyperthermia are magnetite (Fe_3O_4) and maghemite (γ-Fe_2O_3).[6,25,144] This is due to their magnetic properties as well as being considered biocompatible and biodegradable.[22,42] Iron oxides can behave as multi-domain particles, single-domain particles, or as superparamagnets as the particle diameter decreases. The transition from superparamagnetism to single-domain particles is thought to occur around 20-30 nm depending on the material.[145] For maghemite it has been estimated that the critical diameter above which particles contain multiple domains is 166 nm.[113] Magnetite theoretically transitions to multi-domain particles at 80-100 nm.[145,146] Since, the transition to multi-domain particles is above the size range of particles of interest for magnetic hyperthermia, they are not discussed in detail.

Superparamagnetism can be defined as a collection of non-interacting magnetic moments that respond when the thermal energy (K_BT) exceeds the anisotropic

energy.[91,112,124] Superparamagnetism arises because the collective magnetic moments of the entire particle is considered, possibly as high as 10^4-10^5 Bohr magnetons, rather than an individual atom's magnetic moment and therefore very high magnetic saturation and susceptibility is observed.[25,124] Superparamagnets respond to thermal fluctuations when the thermal energy surpasses the anisotropic energy altering the direction of the magnetic moments.[124] These particles will eventually reach an equilibrium similar to thermal equilibrium.[124] The size at which superparamagnetism is reached is called the superparamagnet limit and varies depending on the material.[25,91] The hysteresis loop for a superparamagnet (**Figure 2.2.**) has negligible coercivity, the magnetic field strength required to force magnetization to zero, and negligible magnetic remanence, the remaining magnetism after removing the magnetic field.[25,91,124] These properties allow for excellent magnetic hyperthermia applications as the nanoparticles respond quickly to changes in magnetic field which are present due to the alternating current magnetic field in the radiofrequency range. Superparamagnet iron oxide nanoparticles are also ideal for biomedical applications due to their low probability of aggregation due to any remnant magnetism at room temperature.[25,91] Metallic nanoparticles have higher magnetization values than metal oxide nanoparticles, however they are toxic in most biomedical applications.[91]

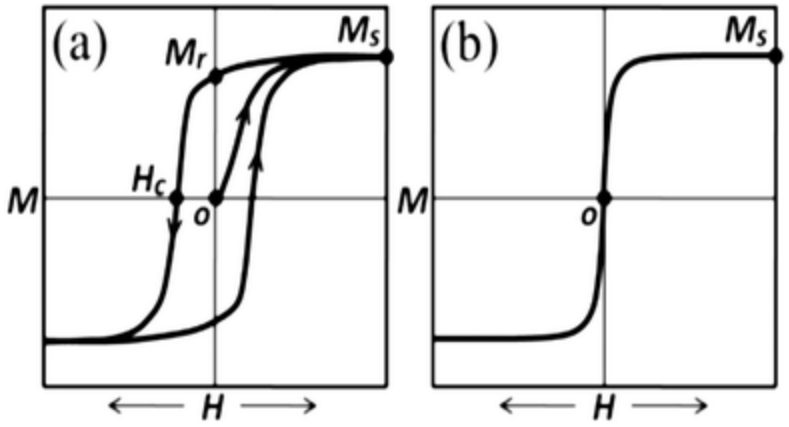

Figure 2.2. Representative hysteresis loop for single domain ferromagnetic (a) and superparamagnetic (b) crystals plotted as magnetization (M) versus magnetic field (H). M_S, M_r, and H_c correspond to magnetization saturation, remnant magnetization, and coercive field respectively. From [123]

Nanoparticles with diameters above the superparamagnet limit are considered to be single domain particles.[91,124] Single domain particles have a uniform spin direction and do not contain domain walls allowing for large magnetic coercivities due to lack of domain walls.[91,112,124] Due to the reduced magnetostatic energy at sufficiently small volumes the multiple domain walls are energetically unfavorable.[112] Additionally, shape anisotropy can increase the coercivity of single domain nanoparticles.[91] On the single domain size range it is energetically favorable to allow for external magnetostatic energy rather than create domain walls.[91] Thus larger particles will form multiple domains separated by domain walls.[91,112] The energy of exchange, anisotropy and magnetostatic interactions determines the size and shape of each domain within the larger or bulk material.[112]

Chapter 3: Benzyl Alcohol Synthesis of Iron Oxide Nanoparticles

3.1 Experimental Section

3.1.1 Reagents, Materials, and Equipment

All chemicals and materials were used as received. Tetramethylammonium hydroxide (TMAOH) solution (Alfa Aesar, 25% w/w aq.), copper TEM grids (Ted Pella Inc., 200 mesh Formvar carbon type B), Fe inductively coupled plasma (ICP) standard (Alfa Aesar, Iron, plasma standard solution, Specpure®, Fe 1000 µg/mL), hydrochloric acid solution (HCl) (Electron Microscopy Sciences, 2%), potassium ferrocyanide aqueous solution (Prussian Blue) (Electron Microscopy Sciences, 2%), two-neck 100 mL round bottom flask (Chemglass), coil style reflux condenser (Chemglass), iron (III) acetylacetonate ($Fe(acac)_3$) (Acros Organics, 99+%), benzyl alcohol (Alfa Aesar, 99%), and acetone (Fisher Scientific, ACS grade)

3.1.2 Modified Seed Growth of Iron Oxide Nanoparticles

Iron oxide nanoparticles were synthesized under nitrogen flow or open to air in a two-neck 100 mL round bottom flask (Chemglass) equipped with a coil style reflux condenser (Chemglass). First, iron (III) acetylacetonate ($Fe(acac)_3$) (2, 4, or 6 g) (Acros

Organics, 99+%) was dissolved in benzyl alcohol (20 mL) (Alfa Aesar, 99%) under constant magnetic stirring. The solution was stirred vigorously and immediately heated to reflux. For syntheses conducted under nitrogen flow the nitrogen was initially bubbled in the benzyl alcohol and $Fe(acac)_3$ for 30 minutes before heating to reflux. Upon color change from dark red to black, the reactions were carried out for 2 or 24 hours. The reaction was removed from heat and stirred for 15 minutes to allow for cooling. The resultant iron oxide nanoparticles were precipitated in acetone (Fisher Scientific, ACS grade) and extracted by magnetic separation. Washing with acetone was repeated 3-5 times with brief sonication (Cole Parmer, Ultrasonic Cleaner 8892) between washes. Flowing nitrogen was used to dry the nanoparticle product to a fine powder.

For the modified seed growth procedures, $Fe(acac)_3$ (2, 4, or 6 g) was dissolved in benzyl alcohol (20 mL) in a round bottom flask under a coil style reflux condenser, stirred vigorously and heated to reflux, as described above. At 2 or 24 hours of reaction time a second addition of $Fe(acac)_3$ (2, 4, or 6 g) was added, as a solid powder, directly to the hot reaction and continued to react for 2 or 24 hours.

For reactions where precise control of temperature was required, the heating mantle (Thermoscientific, electrothermal heating mantle) was replaced with a silicone oil bath (Alfa Aesar) and temperature controlled by the magnetic stirring hot plate (VWR, VMS-C7) equipped with a temperature control unit (VWR, VT-5 S40). To determine important temperature thresholds, the temperature and color of the solution was monitored and recorded every minute until reaching the desired reaction temperature and the solution color changed completely to black indicating high levels of nanoparticle formation. Reactions were heated at the highest ramp rate obtainable by the heating

mantle or hot plate and oil bath. Products from the seed growth were cooled and washed under the same conditions as all other reactions listed above.

3.2 Characterization Techniques

3.2.1 X-ray Diffraction (XRD)

X-ray diffraction (XRD) is a characterization technique that can be used to determine the crystal structure of a material without destroying the sample.[135,147-150] The bulk crystalline structure of a material can be determined by investigating the diffraction pattern resulting from x-rays interacting with the sample.[149,150] To accomplish this, electromagnetic radiation in the form of x-rays with a typical wavelength (λ) of about 0.1 nm are used to probe the atoms of the crystal.[135,150] The wavelength is comparable to the interatomic distance of atoms in the crystal and thus the atoms can elastically scatter the x-rays.[135,149,151] The scattered x-rays will constructively and destructively interfere producing a diffraction pattern that is used to determine the crystal structure of a crystalline material.[135,149,150] The consistent collections of atoms throughout a crystalline material will elastically scatter incident x-rays at certain angles and depending on the distances between the atoms of the lattice the scattered x-ray wave will constructively interfere in specific directions.[135,149] Bragg's law, **Equation 3.**, defines the incident angle (θ), and distance between atomic planes of the lattice (d_{hkl}), where elastically scattered x-rays will constructively interfere for an incident x-ray with wavelength (λ) and spaced at integer multiples (n) of the path difference.[135,149]

$$n\lambda = 2d_{hkl}\sin\theta \quad (3)$$

The peak positions of the resulting XRD pattern are used to determine the lattice parameters, size and symmetry, however to determine the organization of atoms the peak intensities of the diffractions are used.[149] Often the investigator has an idea of the composition of the crystal and so the peak positions and intensities of the diffraction pattern are compared to known crystallography data in order to verify crystal structure.[149] Powder XRD utilizes a large collection of crystals, the powder, which allows the incident x-ray to interact with the sample at numerous angles or orientations at the same time.[150] The powder allows all possible crystal orientations to be investigated by a diffractometer.[150] This produces diffraction cones which are used to determine the diffraction pattern.[150] It is important to note that XRD cannot be used to distinguish magnetite from maghemite as their diffractograms are identical.[135]

XRD line broadening can be used to determine the crystallite size of iron oxides.[135] The Scherrer formula, **Equation 4.**, is used to calculate the crystallite size using the corrected peak width at a certain angle in the XRD measurement, however it underestimates the size for crystals with multiple crystallites.[135] The coherently scattering domain that is perpendicular to the hkl plane (MCL_{hkl}) gives the mean crystallite size, however this is biased towards larger crystallites as they more intensely scatter.[135]

$$MCL_{hkl} = \frac{K\lambda}{b\ \cos\theta} \tag{4}$$

In the Scherrer formula K is a shape factor, b is the full width half maximum (FWHM) of the peak being measured, and λ is the wavelength of the x-ray.[135] The value of b is corrected for instrument error by subtracting the instrument width.

Powder x-ray diffraction (XRD) patterns were obtained on a PANalytical X'Pert Pro Materials Research Diffractometer. Dried samples (~ 300 mg) were mildly ground to obtain a fine powder. The fine powder was transferred to a low background silicon disk. XRD patterns were scanned at 20-80° 2θ using a Cu Kα x-ray source and evaluated using X'Pert High Score Plus software. The Scherer equation was used to calculate the crystallite size from peak broadening of diffraction peaks. Standard deviation of the crystallite size was calculated from several peaks of the XRD pattern.

3.2.2 Dynamic Light Scattering (DLS)

Dynamic light scattering (DLS) is used to characterize particles in solution. Particles ranging from 1 nm to 5 μm can be analyzed. The hydrodynamic size , size distribution in terms of the polydispersity index (PDI), and the diffusion coefficients of particles in solution can all be measured using DLS.[152,153] The basic principle of DLS involves probing a colloidal suspension with a monochromatic light source and then recording the time variation of the intensity of the light scattering by the nanoparticles that are diffusing in a solution.[152,153] The intensity autocorrelation function is then used to express this data in terms of the correlation between the intensity measured at one time point and the intensity after a delay in time.[153] The diffusion coefficients are used to calculate the hydrodynamic diameter and PDI values.[153] The diffusion coefficient can be measured since the nanoparticles in solution have kinetic energy.[152] The scattering intensity of light for scattering angles over time relates to the diffusion of the nanoparticles through the solution.[152] Thus, several parameters such as viscosity and refractive index of the solution need to be known in order to effectively characterize the

nanoparticles size. The basic equation utilizes the range of scattering angles (θ_{DLS}), refractive index (n), and the incident light's wavelength in a vacuum (λ) to calculate the magnitude of the scattering wave (q) shown in **Equation 5**.[152]

$$q = \left(\frac{4\pi n}{\lambda}\right) sin\left(\frac{\theta_{DLS}}{2}\right) \quad (5)$$

Utilizing the Stokes-Einstein equation (**Equation 6.**) the hydrodynamic radius (R_H) can be determined for spherical particles, where K_B is Boltzmann constant, T is the solution temperature, and η is the medium viscosity.[152,153] The hydrodynamic radius is directly related to the diffusion coefficient (D_f) which is the diffusion of the nanoparticles through the medium it is dispersed within.[152]

$$D_f = \frac{K_B T}{6\pi\eta R_H} \quad (6)$$

The PDI value is calculated from the average decay rate (⟨Γ⟩) and the variance of the decay rate distribution (μ_2) as shown in **Equation 7**.[152]

$$PDI = \frac{\mu_2}{\langle\Gamma\rangle^2} \quad (7)$$

Since, true monodispersity is unlikely the calculated ⟨Γ⟩ and q values from the correlation function can then be used to calculate the average hydrodynamic radius as shown in **Equation 8**.[152] Thus, a weighted function can be used depending on the instrument used that will calculate the summation of all possible decay rates for each particle and will relate this to a size distribution.[153] Since this is a weighted average it is best to use this value as a "semi-quantitative" representation of the size distribution rather than the exact size distribution.[153]

$$R_H = \frac{K_B T}{6\pi\eta\langle\Gamma\rangle} q^2 \quad (8)$$

Since this data is a collection or average of the measured nanoparticles in solution the data can be presented as based on number, volume, or intensity. The intensity values will be biased towards larger sized nanoparticles as they will more intensely scatter light. Therefore, the volume and/or number measurements are often more indicative of the true hydrodynamic diameter.

DLS can also be used to determine the thickness of surface functionalities added to the nanoparticles. To do this the hydrodynamic diameter determined for the nanoparticles with and without the surface functionalization are measured and then subtracted. This characterization technique offers a rapid and easy method for indirect measurement of particle size in solution, thickness of surface functionalization's, and measure of polydispersity based on number, intensity, or volume measurements.[152] It has the added benefit of being a nondestructive technique.[152]

The hydrodynamic diameters and polydispersity indexes of iron oxide nanoparticles were analyzed at ambient conditions using a Malvern Zetasizer Nano-ZS (Malvern Instruments, U.K.). The DLS light source used was a He-Ne laser (633 nm, max 4 mW). Iron oxide nanoparticles (20 mg/mL) were dispersed in tetramethylammonium hydroxide (TMAOH) solution (0.25%) and sonicated for 180 minutes. After sitting overnight a 1:100 dilution (0.01 mL diluted in 0.99 mL H_2O) was made for DLS analysis. Samples were then transferred to a low volume disposable cuvette and hydrodynamic diameter and PDI values were calculated as an average of 5 runs containing 11 measurements per run.

When measuring the hydrodynamic diameter of nanoparticles dispersed in TMAOH it was important to verify that the hydrodynamic diameter and PDI did not

significantly change based on the concentration of TMAOH. This is important to determine as nanoparticles with different particle sizes may require different concentrations of TMAOH for dispersion. The hydrodynamic diameters and PDI of nanoparticles produced from a modified seed growth dispersed in various concentrations of TMAOH are shown in **Table 3.1**.

Table 3.1. Initial hydrodynamic diameters and PDI values for various v/v % concentration of TMAOH.

% TMAOH	Hydrodynamic Diameter (nm)	PDI[a]
0.0625	25.99	0.38
0.125	29.96	0.363
0.25	23.61	0.39
0.5	26.12	0.41

[a]Polydispersity Index (PDI) determined by DLS.

3.2.3 Vibrating Sample Magnetometry (VSM)

Vibrating sample magnetometry (VSM) can be used to determine the type of magnetism based on the hysteresis loop produced. A representative ferromagnetic and superparamagnetic hysteresis loops are displayed in **Figure 2.2**. To produce a hysteresis loop a sample is loaded into a magnetometer and the external magnetic field applied starts at zero and is increased until the magnetization becomes saturated or reaches a magnetization maximum.[135,150] The magnetization saturation is the point at which all of the magnetic moments are aligned in accordance with the direction of the

externally applied magnetic field.[135,150] At this point the external magnetic field direction is reversed and the magnetization is recorded until it reaches the saturation magnetization point for the “negative” external magnetic field.[135,150] To complete the hysteresis loop the external magnetic field direction is then reversed again and returned to the “positive” external magnetic field maximum where the initial saturation magnetization was reached. The shape, height, and width of the loop are all indicative of the materials type of magnetism.

Information gained from magnetometry includes the saturation magnetization (M_s), remnant magnetization (M_r), initial magnetic susceptibility (X), and coercivity (H_c). The saturation magnetization is when all of the magnetic moments are oriented in the same direction or saturated and thus the magnetization does not increase with increasing magnetic field strength applied.[135,150] The remnant magnetization is the amount of magnetization remaining after the external magnetic field (H) is returned to zero.[135,150] The magnetic field required to return the magnetization to zero or demagnetize is termed the coercivity or coercive field.[135,150] The initial magnetic susceptibility is determined from the initial linear increase in magnetization as the external magnetic field applied increases.[135] Samples containing magnetite and maghemite will overpower the magnetic properties of other iron oxides detected in magnetometry due to their ferrimagnetic properties.[135]

Magnetic characteristics were probed using a VersaLab 3 Tesla Cryogen-Free Vibrating Sample Magnetometer (VSM) (Quantum Design). Samples were prepared by weighing dry samples (5-15 mg) and sealing in a sample capsule (Quantum Design). VSM sample capsules were loaded and scanned for offset at 35 mm. Moment versus

field measurements were conducted at <50 Torr purged pressure, a sweep rate of 150 Oersted/ second (Oe/s) with no automatic centering and scanning 5 quadrants from 0 Oe to 15,000 Oe (Hmax) to -15,000 Oe (Hmin). Saturation magnetization was determined from the magnetization versus magnetic field strength plots at Hmax or Hmin. Samples were mass corrected with thermogravimetric analysis (TGA).

3.2.4 Thermal Gravimetric Analysis (TGA)

Thermal gravimetric analysis is a thermoanalysis characterization method that is routinely used to analyze the weight loss of a material depending on the temperature applied.[135] Typically, samples are weighed on a highly sensitive balance and the weight is recorded as the temperature is increased at a rate of 2-10 °C/min.[135] This technique is useful in determining the mass of impurities in a sample. Such impurities can include water content, organic compounds, surface functionalities, or chemicals used in synthesis or wash steps that were not adequately removed. This can be expressed in terms of mass percent loss. The mass percent remaining is used to correct the mass of the sample used in other characterization techniques where mass of the pure material is important, such as VSM.

To determine mass corrected values, thermogravimetric analysis (TGA) was run on a Q5000 TGA (TA Instruments). Dry samples (5-50 mg) were loaded on platinum pans and the temperature was ramped at 10 °C/min from room temperature to 150°C and held isothermal for 15 minutes. Subsequently, ramping was continued at 10 °C/min to 400°C and held isothermal for 60 minutes. TGA was run under a nitrogen flow rate of 25 mL/min.

3.2.5 Transmission Electron Microscopy (TEM)

Transmission electron microscopy (TEM) utilizes a beam of electrons to obtain an image with atomic scale resolution.[153,154] The electrons are produced by a hot filament, which are then accelerated by an electron gun, and the beam is then focused by several electro-magnets.[153,154] The beam of electrons will then interact with the sample and the intensity of the transmitted electron beam will be affected by diffraction, atomic number, and phase contrast.[154] Therefore it is important to use a sample stage with properties different than the sample to maximize the contrast for higher resolution images.[153,154]

Bright field TEM images of iron oxide nanoparticles were obtained with a Zeiss LIBRA® 120 PLUS TEM. Samples were prepared for TEM by drying 1:10 dilution of iron oxide nanoparticles in 0.25% TMAOH solution (2 mL; 20 mg/mL) on copper TEM grids (Ted Pella Inc., 200 mesh Formvar carbon type B). Images of CMPVA functionalized iron oxide nanoparticles were loaded at a 1:10 dilution after all clean up and filtering processes described above. Nanoparticle size measurements were performed using Image J software.

3.2.6 Radiofrequency Heating

The heating properties of iron oxide nanoparticles synthesized by different parameters were investigated using 1.2-2.4 kW EasyHeat induction heating system with a coil designed at a set point of 200 Ampere (A) to run at 1222 watt (W) and frequency

(f) of 269 kHz to produce an alternating magnetic field with a magnetic field strength (H) of 37.4 kA/m at 175.4 A. The magnetic field strength of a coil can be calculated from Ampere's law for a solenoid as shown in **Equation 9.**[155] Where B is the magnetic field, L is the length of the coil, N is the number of turns in the coil, I is the current, and μ_o is the permeability of free space.

$$BL = \mu_o N I_o \tag{9}$$

Using **Equation 10.**[150] to relate the magnetic field to magnetic field strength (H) we can determine a reasonable approximation for the magnetic field strength inside the coil, by substituting into **Equation 9.** to give **Equation 11.** The coil used, in determining RF heating properties, has N= 8 turns and a L=0.0375 m which corresponds to H= 37.4 kA/m at 175.4 A.

$$B = \mu_o H \tag{10}$$

$$H = \frac{N}{L} I_o \tag{11}$$

The temperature of the solution being exposed to the RF AC magnetic field was measured *in situ* with an OpSens fiber optic temperature sensor and recorded by SoftSens software. Initial tests were performed on iron oxide nanoparticles in 0.25% TMAOH aqueous solution (3 mL; 20 mg/mL) to characterize the ability of the iron oxide nanoparticles to heat in solution. The RF heating was conducted at 175.4 A, and H=37.4 kA/m for 600 seconds and the temperature was recorded every 1.4 seconds. To account for convection heating, water (3 mL) was measured under the same conditions. The temperature rise was constant over the entire 600 s with a dT/dt value of 0.549°C. This value was used to correct the initial linear temperature rise of RF heating of iron oxide TMAOH samples.

RF heating values are corrected for the concentration of iron as determined by a Prussian Blue assay. A standard curve was produced by Prussian Blue UV-Vis absorption assay (λ=715 nm) with a Fe inductively coupled plasma (ICP) standard (Alfa Aesar, Iron, plasma standard solution, Specpure®, Fe 1000 µg/mL) and UV-Vis absorption with a Nanodrop 2000c spectrometer (Thermo Scientific). The RF heating samples were first diluted 1:100. Then samples (10 µL) were mixed with HCl (10 µL; 2%) (Electron Microscopy Sciences) and Prussian Blue (20 µL; 2%) (Electron Microscopy Sciences). After exactly 15 minutes of incubation at room temperature UV-Vis absorption of prepared samples (2 µL) was measured with no baseline correction.

3.3 Results and Discussions

3.3.1 Investigation of Synthesis Parameters

Several synthetic parameters such as temperature, concentration, time and addition of extra iron precursor were investigated to optimize the iron oxide nanoparticles for magnetic fluid hyperthermia applications. When investigating the reaction concentration the reaction volume of 20 mL of benzyl alcohol was not varied and instead the amount of $Fe(acac)_3$ was modulated.

To keep track of the reaction conditions, the following naming system was utilized. A and B denote the first or second additions of $Fe(acac)_3$ respectively and are separated by an underscore. The A and B are followed by numbers indicating the gram amount of $Fe(acac)_3$ added at the respective addition. This is followed by a “-X” with X indicating the time in hours the reaction proceeded before a subsequent addition. When temperature was investigated as a parameter, it is indicated by the number in

parenthesis beside the reaction time. A2-24(175)_B2-24(175) for example indicates a reaction with 2 g of $Fe(acac)_3$ initially added to 20 mL of benzyl alcohol in the presence of air. This was reacted for 24 hours at 175°C before a second addition of 2g of $Fe(acac)_3$, which was then reacted for an additional 24 hours at 175°C. When the reaction was carried out under nitrogen flow the reaction name starts with a "N_2", for example N_2-A2-24(205) describes a synthesis of 2 g of $Fe(acac)_3$ initially added to 20 mL of benzyl alcohol and reacted for 24 hours at a temperature of 205°C. If a temperature is not provided, all reactions were carried out using a heating mantle at identical temperatures as confirmed by a similar rate of reflux.

Each reaction was characterized using XRD, VSM corrected by TGA, RF heating corrected by Prussian blue analysis, and DLS to determine crystallite size, magnetization saturation (M_S), RF heating, and hydrodynamic diameter and PDI values respectively. The XRD pattern for reactions N_2-A2-24, A2-24, and A2-24_B2-24 are shown in **Figure 3.1**. The XRD patterns of all samples are not shown as they were all indicative of iron oxide material. XRD peak data was used to calculate the crystallite size and these values are shown in their respective sections where they are discussed. All of the RF heating curves are not shown, instead the heating rate calculated from the initial linear temperature increase of the heating curve was measured and corrected for concentration of Fe by Prussian blue analysis. These RF heating values are shown in the tables in their respective sections. Selected RF heating curves are shown in **Figure 3.2.** for deionized water, N_2-A2-24, A2-24, A2-24_B2-24, and A2-24(195)_B2-24(195). A representative DLS pattern and peak data are shown for reaction A4-24(195)_B4-24(195) in **Figure 3.3.** and **Table 3.2.** respectively. The VSM hysteresis loop and TGA

determined weight loss were used to determine the magnetization saturation for reaction A2-24(195)_B2-24(195), as shown in **Figure 3.4.** and **Figure 3.5.** respectively.

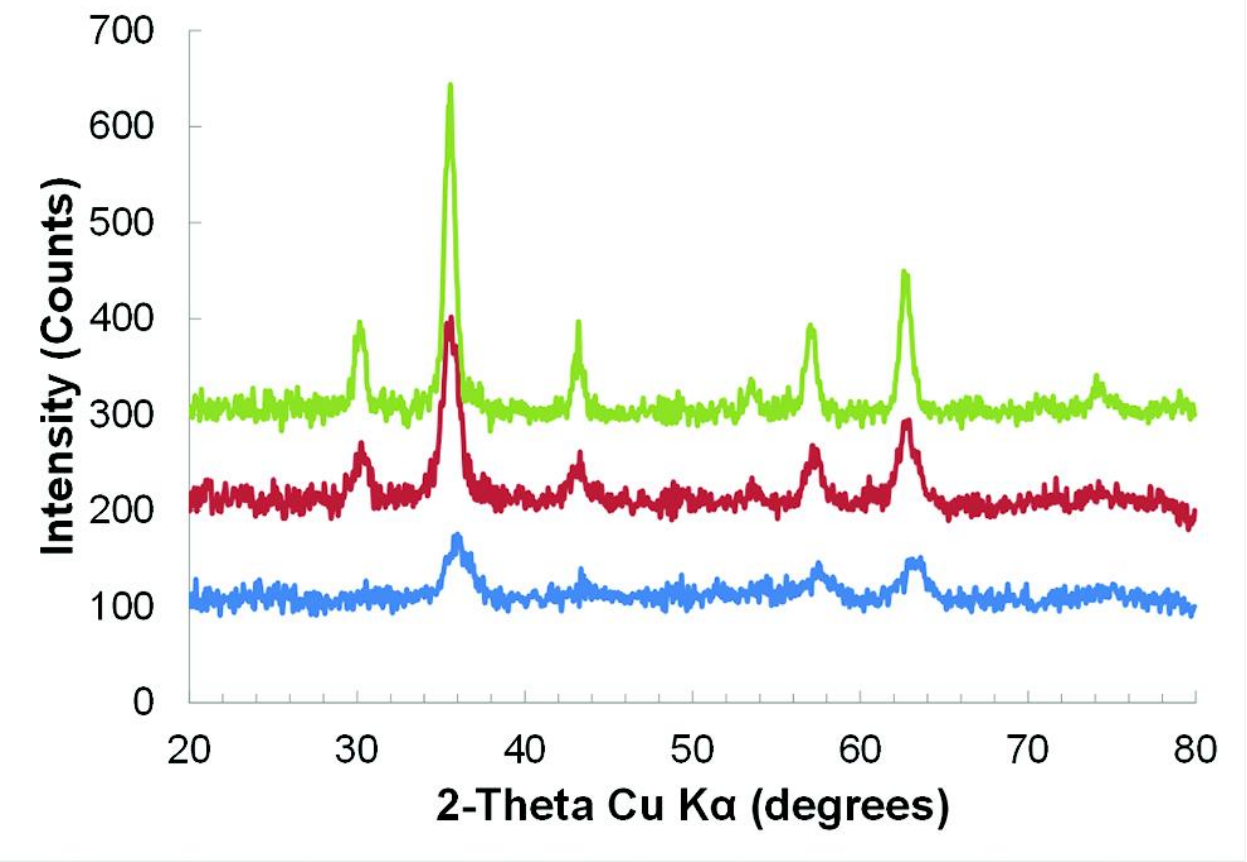

Figure 3.1. XRD analysis of reactions N_2-A2-24 under N_2 (blue), A2-24 (red), and A2-24_B2-24 (green). XRD patterns are offset by 100 count increments.

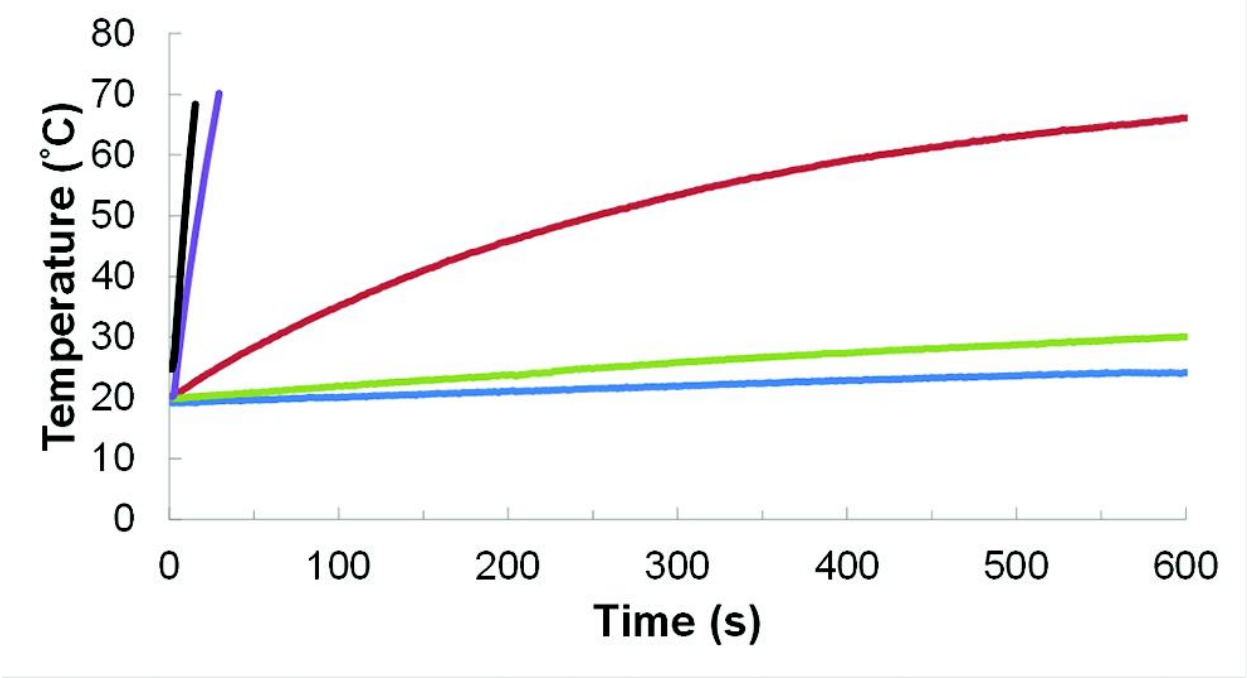

Figure 3.2. Heating curves of 3 mL of water and iron oxide samples dispersed in 0.25% TMAOH. Concentrations of iron determined by Prussian Blue UV-VIS are 0, 14.48, 15.40, 14.00, and 15.36 mg/mL for deionized water (blue), A2-24 under nitrogen (green), A2-24 (red), A2-24_B2-24 (purple), and A2-24(195)_B2-24(195) (black) respectively. An alternating magnetic field 175.4 A at frequency of 270 kHz for 600 seconds was used and the temperature was recorded every 1.4 seconds.

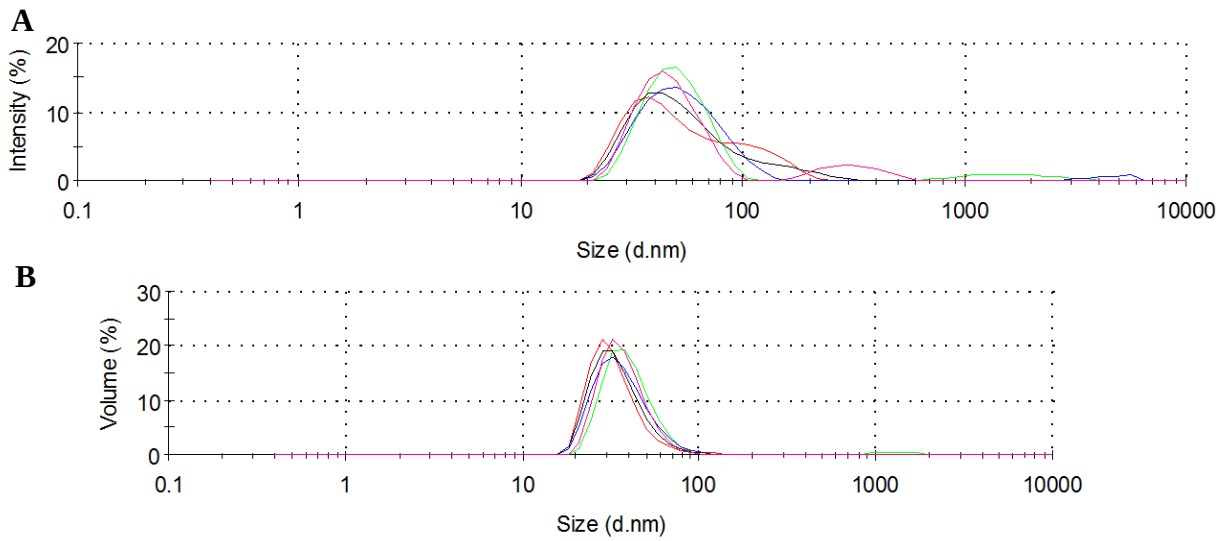

Figure 3.3. The size distribution by percent intensity (A) and size distribution by percent volume (B) for reaction A2-24(195)_B2-24(195). The calculated Z-average hydrodynamic diameter = 47.75 nm and the PDI=0.219.

Table 3.2. Hydrodynamic size, percent composition, and width of each peak for the size distribution by percent intensity and size distribution by percent volume for reaction A2-24(195)_B2-24(195).

Size Distribution by Percent Intensity			
	Hydrodynamic Diameter (nm)	**% Intensity**	**Width (nm)**
Peak 1	47.08	86.8	14.31
Peak 2	313.3	13.2	95.5
Peak 3	0	0	0
Size Distribution by Percent Volume			
	Hydrodynamic Diameter (nm)	**% Volume**	**Width (nm)**
Peak 1	37.52	99.3	11.26
Peak 2	328.1	0.7	109.5
Peak 3	0	0	0

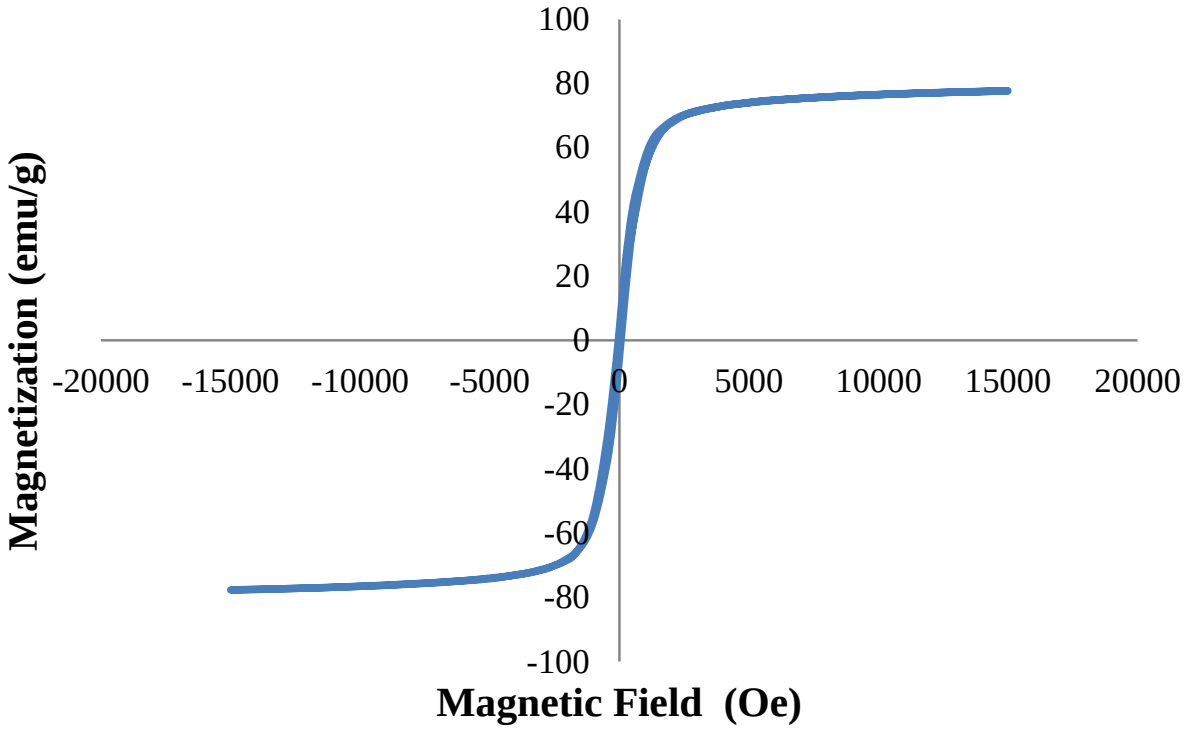

Figure 3.4. Hysteresis loop of 10.303 mg of reaction A2-24(195)_B2-24(195). The mass of 10.901 mg was weight corrected using a weight loss of 5.4836% determined by TGA.

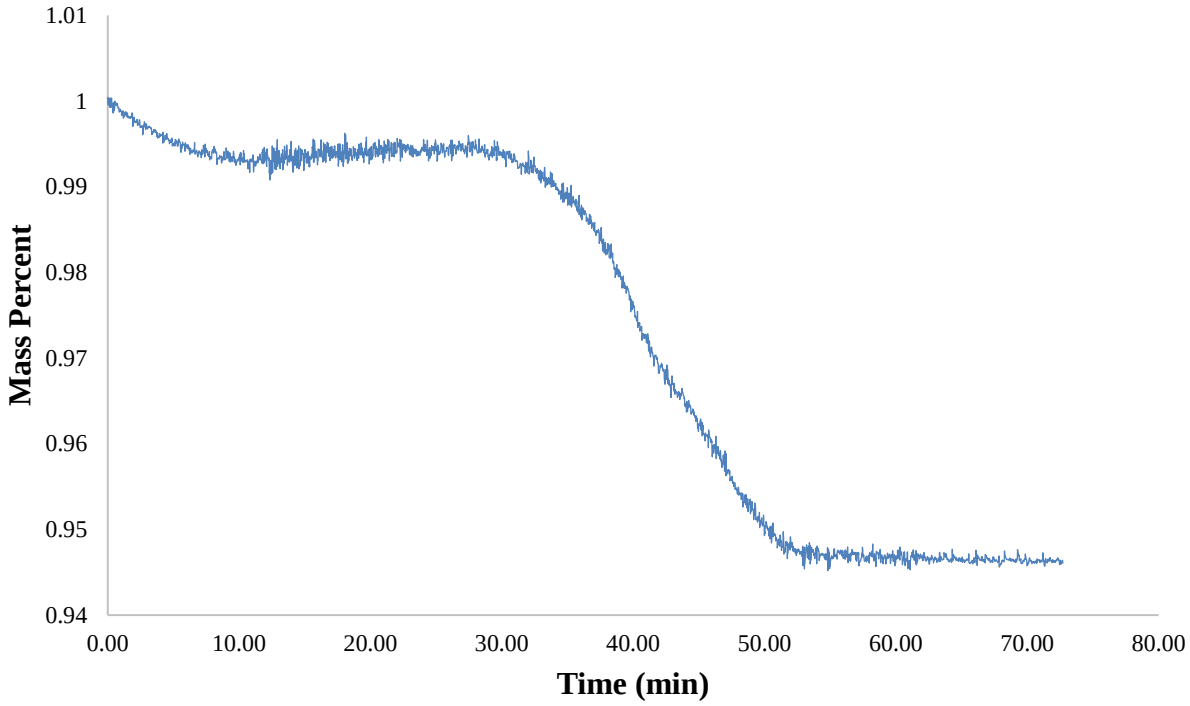

Figure 3.5. TGA of reaction A2-24(195)_B2-24(195) with a final mass percent of 0.945164 at 400°C.

3.3.2 Effect of Reaction Environment

Iron oxide nanoparticles were first synthesized in benzyl alcohol under nitrogen flow. The use of nitrogen or argon flow is often the standard method in the literature when carrying out thermal decomposition of $Fe(acac)_3$ or iron carboxylate salts.[49,97,109,156-160] N_2-A2-24 was the first reaction conducted under nitrogen using the heating mantle. This resulted in nanoparticles with a crystallite size of 6.5 ± 1.2 nm as calculated from the powder x-ray diffraction (XRD) pattern in **Figure 3.1.** using the Scherrer equation. The saturation magnetization (M_s) was found to be 53.39 emu/g as measured by vibrating sample magnetometry (VSM) and mass corrected by thermal gravimetric analysis (TGA) data.

As mentioned previously, the optimal crystallite size for magnetic nanoparticle based induction heating has been shown to be around 15 nm. While this is not the overall particle size, and the exact relationship between particle size and heating is not clear, our goal was to use the benzyl alcohol based synthesis to increase the crystallite and particle size into an optimal range for RF heating. Thus, our hypothesis was that the crystallite size could be increased by changing the reaction conditions from nitrogen flow to being open to air. Carrying out the reaction in the presence of air, A2-24, could facilitate the oxidation of benzyl alcohol to benzaldehyde and reduction of $Fe(acac)_3$ at temperatures further below the start of thermal decomposition, similar to the mechanism of metal and metal oxide nanoparticle formation in glycols.[48,87-89,161] Reactions carried out open to air had reflux drips beginning around 178°C and increased in frequency as the temperature was increased to 205°C. These reflux drips suggest the formation of benzaldehyde which has a boiling point of 178.1°C.[162] It is probable that benzaldehyde is formed at lower temperatures and thus reduction of iron precursor to form monomers for nucleation is possibly occurring at lower temperatures. Starting the reaction at lower temperatures, where the temperature ramp rate is faster, would allow for fewer nuclei to form and a better separation of nucleation and growth phases; both of which would lead to larger nanoparticles and potentially a larger crystalline core.[35] This simple reaction parameter change resulted in iron oxide nanoparticles with a crystallite size of 8.33 ± 0.393 nm (**Figure 3.1.**) and a M_s of 70.839 emu/g. Typically, the thermal decomposition of $Fe(acac)_3$ starts to occur around 170-180°C depending on the solvent.[163] Nanoparticle formation, indicated by a color change from dark red to black, initially occurred under nitrogen at 174.4°C after 31 minutes and the reaction solution appeared

completely black after 40 minutes (**Figure 3.6A.**). In contrast, carrying out the reaction under air with identical heating rate and final temperature resulted in an initial color change at 169.4°C after 20 minutes and a completely black solution at 30 minutes (**Figure 3.6B.**). This indicates that the presence of oxygen leads to the reaction initiation occurring sooner in time and at a lower temperature, suggesting the possibility of an additional mechanism by which the iron oxide nanoparticles are forming in benzyl alcohol. In order to verify if the benzyl alcohol was acting as a reducing agent in this synthesis, $FeCl_2$ was used as a precursor in place of the $Fe(acac)_3$ with the addition of sodium hydroxide, NaOH, as in glycol synthetic methods.[48,87,89,161] This reaction produced iron oxide under both air and N_2 (**Figure 3.7.**) confirming the presence of another mechanism of nanoparticle formation in benzyl alcohol other than thermal decomposition of $Fe(acac)_3$. As with the $Fe(acac)_3$ synthesis, the $FeCl_2$ reaction under air had an initial color change at 90.8°C compared to 99.3°C for N_2, and turned completely black under air at 127.7°C versus 132.7°C for the reaction under N_2 (**Figure 3.6C and D**). Therefore, these results suggest that running the reaction under air promotes the earlier initiation of nucleation, giving further separation of nucleation and growth which led to the increase in crystallite size. From this mechanistic insight, all additional syntheses to increase size were primarily carried out under air.

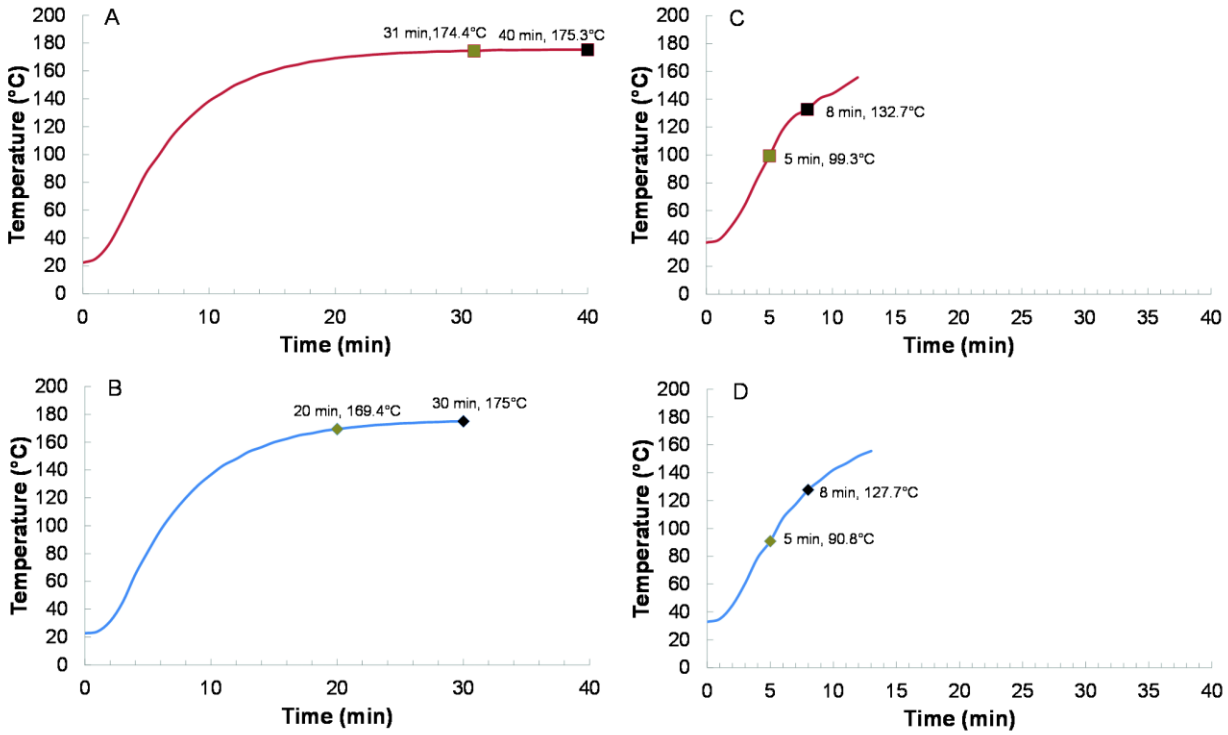

Figure 3.6. Heating curves for reaction of $Fe(acac)_3$ in Benzyl Alcohol heated to 175°C under nitrogen (A), and air (B). Heating curves for reaction of $FeCl_2$, NaOH, and Benzyl Alcohol heated to 150°C under nitrogen flow (C), and air (D). Initial color change is denoted with a golden brown square (nitrogen) or diamond (air), and nanoparticle formation upon solution turning black is indicated by a black square or diamond.

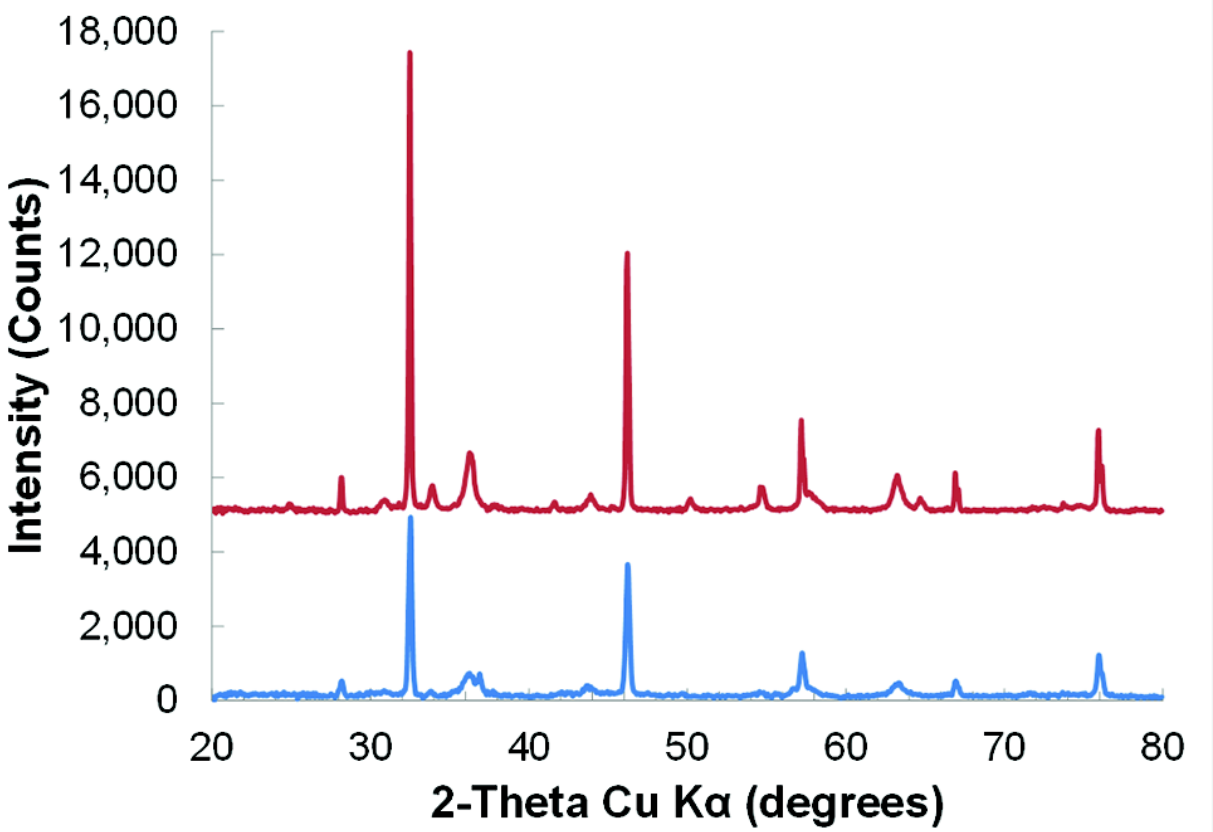

Figure 3.7. XRD analysis of nanoparticles produced by reacting $FeCl_2$, NaOH, and Benzyl Alcohol under nitrogen flow (blue), and air (red). XRD patterns are offset by 5000 count increments. Peaks at 32.5 and 46.2 are thought to be sodium chloride, NaCl. The reaction under nitrogen was composed of 71% NaCl and 29% iron oxide. The reaction under air was composed of 77% NaCl and 23% iron oxide.

3.3.3 Effect of Reaction Time

One of the disadvantages of the benzyl alcohol synthesis or thermal decomposition syntheses is that longer reaction times are generally required to produce larger crystallites with smaller size distributions. Aqueous co-precipitation for example can produce iron oxide nanoparticle on the order of a few minutes, but typically have

very large size distributions. To investigate if the benzyl alcohol synthesis could produce larger crystallites with lower PDI values and similar RF heating characteristics the reaction was carried out for 2 hours and compared to A2-24 as shown in **Table 3.3.**

Table 3.3. Nanoparticle characterization of reactions with different reaction times. Saturation Magnetization, Heating Profile, and Average Size determined by VSM, Heating Induction, XRD, and DLS.

Reaction	Magnetization (emu/g)[a]	RF Heating ([°C/min]/mg)[b]	Crystallite size (nm)	Hydrodynamic Diameter (nm)	PDI[c]
A2-2	60.6	0.03	5.7 ± 0.76	10.93	0.311
A2-24	70.84	0.17	8.8 ± 0.61	13.64	0.703

[a]mass unit indicates grams of iron oxide nanoparticles corrected by TGA.
[b]mass unit indicates milligrams of Fe determined by Prussian blue assay.
[c]Polydispersity Index (PDI) determined by DLS.

As can be seen A2-2 produced iron oxide nanoparticles with a smaller crystallite size of 5.7 ± 0.76 nm and a lower PDI of 0.311 when compared to A2-24. While the lower PDI value is advantageous it is outweighed by the disadvantageous smaller crystallite size and lower magnetization saturation value which is reflected in the much smaller RF heating of 0.03 [°C/min]/mg. While these results reveal a possible way to lower PDI, shorter reaction times do not produce larger crystallite sizes closer to the desired 15 nm which is the most vital nanoparticle property in increasing the RF heating properties of the iron oxide nanoparticles.

3.3.4 Effect of Reaction Temperature

It has been shown that higher temperatures are required for sustained growth of crystallite.[86,88] Benzyl alcohol has a boiling point of 205°C[162] and therefore it is possible that carrying out the reaction at increasing temperatures up to 205°C would result in nanoparticles with slightly larger crystallites. Investigation of the reaction temperature was conducted for syntheses under air and nitrogen environment for two reasons. The first reason was to further increase the crystallite size and magnetization saturation, while decreasing the PDI values in order to increase the RF heating properties. The second reason was to better elucidate the possible mechanism of nucleation and growth.

The nitrogen syntheses reacted at various temperatures ranging from 150-205°C and are shown in **Table 3.4.** These syntheses showed color change from red to black after longer periods of time and at higher temperatures when compared to reactions conducted in the presence of air. Additionally, when the reaction was carried out at the highest temperature of 205°C, reflux drips were not present. This suggests that the benzyl alcohol is not undergoing oxidation to benzaldehyde and thus not reducing the $Fe(acac)_3$. Without the redox reaction occurring, it is highly probable that thermal decomposition of $Fe(acac)_3$ is the main mechanism of formation of monomers for nucleation and growth. In addition, without the reduction of Fe^{3+} to Fe^{2+} it is unlikely that magnetite is forming, which could explain the lower magnetization saturation values (48.54-57.69 emu/g) for nitrogen syntheses. Maghemite has lower magnetization saturation values than magnetite for both nanoscale and bulk materials.[164] Therefore,

nitrogen syntheses in benzyl alcohol may only be producing maghemite. There may be differences of RF heat generation between maghemite and magnetite nanoparticles.

Table 3.4. Nanoparticle characterization of reactions conducted at different temperatures under nitrogen flow. Saturation Magnetization, Heating Profile, and Average Size determined by VSM, Heating Induction, XRD, and DLS.

Reaction	Magnetization (emu/g)[a]	RF Heating ([°C/min]/mg)[b]	Crystallite size (nm)	Hydrodynamic Diameter (nm)	PDI[c]
N_2-A2-24	53.39		6.47 ± 1.17	23.23	0.351
N_2-A2-24(150)	48.54*	0.01	5.65 ± 0.76	13.02	0.372
N_2-A2-24(175)	57.69	0.04	6.06 ± 0.52	11.51	0.306
N_2-A2-24(195)	57.09*	0.02	6.3 ± 0.89		
N_2-A2-24(205)	57.56*	0.05	11.3 ± 0.73	38.48	0.152

[a]mass unit indicates grams of iron oxide nanoparticles corrected by TGA.
[b]mass unit indicates milligrams of Fe determined by Prussian blue assay.
[c]Polydispersity Index (PDI) determined by DLS.
*VSM data was corrected using 0.88 percent weight of sample

An interesting result from the data in **Table 3.4** is that the crystallite size did not increase until synthesized at 205°C. The large increase in crystallite size of 6.3 nm to 11.3 nm when increasing the temperature from 195°C to 205°C further suggests that the reaction is occurring by thermal decomposition only, and is unable to produce highly crystalline materials without sufficient energy that is supplied at these elevated temperatures. The PDI values also decrease to 0.152 at 205°C, suggesting that monodisperse particles can be produced under nitrogen flow in this system only when the temperature is sufficiently high.

When the reaction temperature was increased for the reactions conducted in the presence of air similar trends were observed as compared to nitrogen syntheses with some important differences. The crystallite sizes were larger and magnetization

saturation values were higher. However, the PDI values indicated more polydispersity at lower reaction temperatures. The characterizations of these nanoparticles synthesized under air are shown in **Table 3.5**.

Table 3.5. Nanoparticle characterization of reactions conducted at different temperatures open to air. Saturation Magnetization, Heating Profile, and Average Size determined by VSM, Heating Induction, XRD, and DLS.

Reaction	Magnetization (emu/g)[a]	RF Heating ([°C/min]/mg)[b]	Crystallite size (nm)	Hydrodynamic Diameter (nm)	PDI[c]
A2-24	70.839	0.17	8.8 ± 0.61	13.64	0.703
A2-24(125)	-	-	-	-	-
A2-24(150)	55.50	0.06	6.2	13.58	0.589
A2-24(175)	70.91	0.14	8.9 ±1.39	12.45	0.61
A2-24(195)	74.32	0.18	8.1 ± 0.59	13.3	0.65
A2-24(205)	73.36*	2.76	14.1 ± 0.80	24.53	0.275

[a]mass unit indicates grams of iron oxide nanoparticles corrected by TGA.
[b]mass unit indicates milligrams of Fe determined by Prussian blue assay.
[c]Polydispersity Index (PDI) determined by DLS.
*VSM data was corrected using 0.925 percent weight of sample

Reaction A2-24 produced nanoparticles that had similar characteristics to A2-24(175) and A2-24(195) so it is thought that the margin of error for the heating mantle leads to fluctuating around these temperatures. With temperature controlled precisely using a silicone oil bath, it was found that iron oxide nanoparticles were not produced at 125°C. At 150°C the nanoparticles synthesized had low magnetization saturation values, 55.50 emu/g, comparable to nitrogen syntheses. However, the crystallite size of 6.2 nm was larger than N_2-A2-24(150), but also had a larger PDI value of 0.589. This suggests that both oxidation of benzyl alcohol to benzaldehyde to reduce the iron and thermal decomposition of $Fe(acac)_3$ are occurring which allows for larger crystallite sizes by

better separation of nucleation and growth, but results in larger PDI values caused by some overlap of both mechanisms occurring. It is important to note that the RF heating rate is drastically increased over the RF heating of nitrogen syntheses. This is most likely due to the larger crystallite sizes; however, N_2-A2-24(205) had a crystallite size of 11.3 ± 0.73 nm, and only had a RF heating value of 0.05 [°C/min]/mg. This would suggest that the lower magnetization value of 57.56 emu/g could be limiting the achievable RF heating. The reactions under air with the smallest crystallite size with magnetization saturation values above 70 emu/g have almost triple the RF heating properties as the N_2-A2-24(205) with a larger crystallite size. When the reaction temperature is increased to 205°C the PDI value decreases significantly and the crystallite size almost doubles. It is thought that the reaction encounters a “first stage” where reduction of Fe^{3+} to Fe^{2+} occurs producing initial nuclei by LaMer growth model, but is quickly reached and passed in the 205°C synthesis. When this “first stage” is quickly reached and passed fewer nuclei are formed before growth by diffusion begins due to larger increase in monomer concentration and shorter time for nuclei to form as compared to slightly slower ramp of temperature in reactions with lower final reaction temperatures. In addition, more monodisperse nuclei are produced in the shorter time period in which nucleation is occurring because of the better separation of nucleation and growth. The reaction then encounters the second stage where thermal decomposition and reduction of Fe is occurring allowing for growth on fewer nuclei that have a smaller size distribution which results in larger crystallites and higher monodispersity.

The syntheses conducted under air, can produce larger crystallite sizes at lower temperatures and achieve lower PDI values with better separation of nucleation and growth by utilizing two mechanisms of formation of monomers. This precise control of nanoparticle characteristics is highly advantageous for producing nanoparticles where small differences in nanoparticle properties can drastically affect the RF heating capabilities of the material. The difference is most likely due to syntheses conducted in the presence of air containing both thermal decomposition and redox mechanisms occurring allowing better separation of nucleation and growth. Therefore more precise control of nanoparticles parameters can be achieved when reactions are carried out in the presence of air.

3.3.5 Effect of Reaction Concentration

The initial $Fe(acac)_3$ precursor concentration was increased in an attempt to increase the crystallite size, as some synthetic methods in the literature use this parameter to increase the overall particle size.[165] Increasing the $Fe(acac)_3$ amount by 2 grams per reaction, (A2-24, A4-24 and A6-24) resulted in no significant change in crystallite size, **Table 3.6**. This did however show an increase in the hydrodynamic diameter of 13.64 nm, 14.68 nm and 16.5 nm and decrease in polydispersity index (PDI) values of 0.703, 0.2 and 0.164 respectively (note: lower PDI corresponds to a more monodisperse solution). The increase in overall particle size and decrease in PDI can be rationalized by the LaMer growth model.[166-168] A schematic representation of the LaMer growth model is shown in **Figure 3.8**.

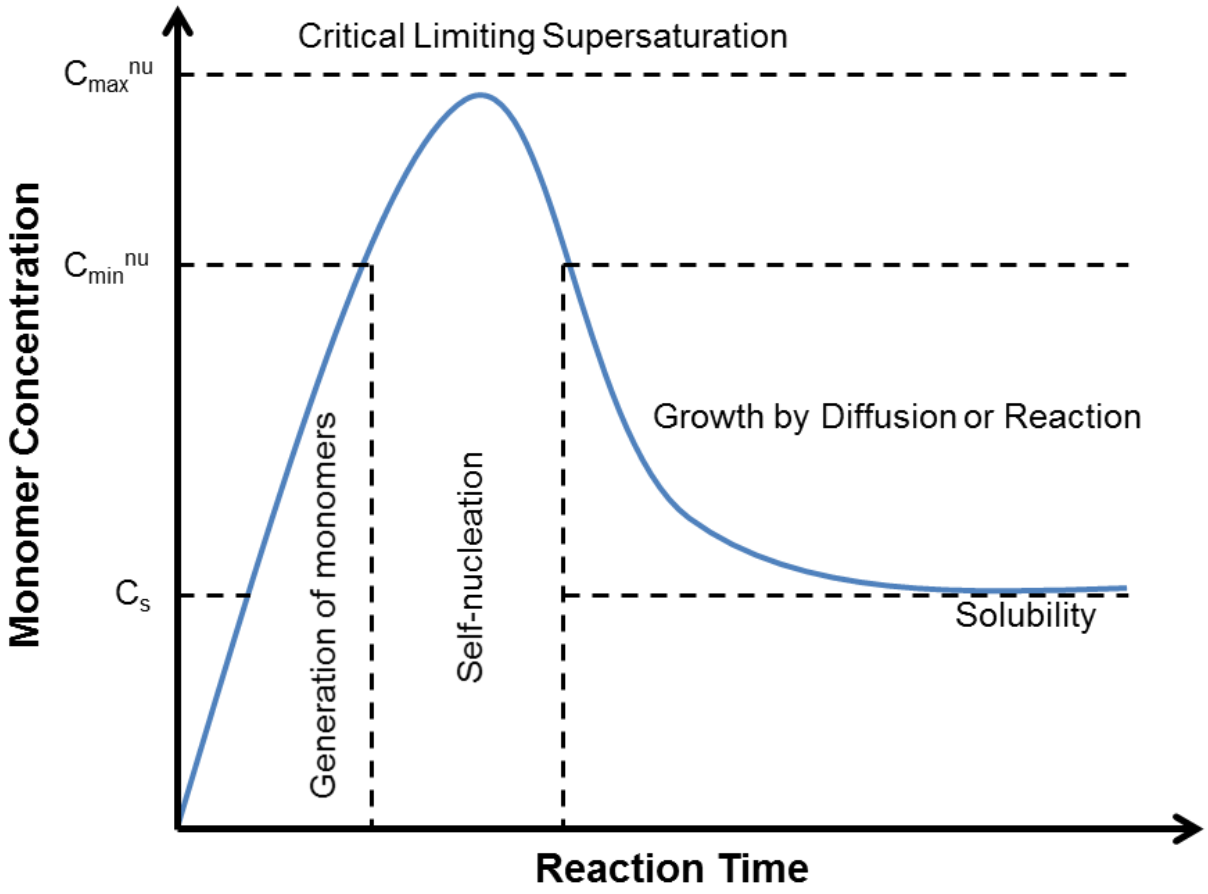

Figure 3.8. Schematic representation of LaMer growth model depicting the generation of monomers, formation of nuclei, and growth by diffusion or reaction. Three concentrations of monomers are denoted as C_S, C_{min}^{nu}, and C_{max}^{nu} representing the concentration of monomers that are stable in solution, the concentration at which nucleation begins, and the concentration where the rate of nucleation becomes infinite, respectively. Adapted from [166].

Increasing the Fe precursor concentration leads to an increased rate of reaching the critical supersaturation concentration for nucleation and the critical limiting supersaturation level.[166-168] At the critical supersaturation concentration for nucleation

the rate of nucleation or the rate at which monomers are used to form nuclei is slow, therefore the concentration will continue to increase towards the critical limiting supersaturation level.[166] As the monomer concentration increases towards this critical limiting supersaturation level the rate at which nucleation occurs increases exponentially until reaching the critical limiting supersaturation level at which point the rate of nucleation becomes infinite.[166] Upon reaching this critical supersaturation, a "burst" nucleation event occurs depleting the concentration of monomers for nucleation below the critical supersaturation concentration thus halting further nucleation.[166,168] Quicker production of monomers will thus lead to reaching higher nucleation rates or a greater "burst" nucleation event which will lead to more monodisperse nanoparticles. Then the reaction switches over to growth with the remaining monomers in solution then growing on the nuclei.[166,168] The growth stage is limited by either diffusion to the surface or reaction rate on the surface until the concentration of monomers decreases to the solubility concentration.[166,168] Once the solubility concentration is reached, Ostwald ripening will occur to lower the surface energy of nanoparticles by dissolving the smaller nanoparticles that will then grow on larger nanoparticles.[172,173] This provides a better separation of the nucleation and growth phases to increase the monodispersity and more available material for the growth phase leading to larger nanoparticles, for reactions A2-24, A4-24, and A6-24, as seen in the results in **Table 3.6**.

Table 3.6. Nanoparticle characterization of reactions with varying precursor concentrations. Saturation Magnetization, Heating Profile, and Average Size determined by VSM, Heating Induction, XRD, and DLS.

Reaction	Magnetization (emu/g)[a]	RF Heating ([°C/min]/mg)[b]	Crystallite size (nm)	Hydrodynamic Diameter (nm)	PDI[c]
A2-24	70.84	0.17	8.8 ± 0.61	13.64	0.703
A4-24	68.99	0.13	8.3	14.68	0.2
A6-24	68.25	0.22	7.9	16.5	0.164
A2-24(205)	73.36*	2.76	14.1 ± 0.80	24.53	0.275
A4-24(205)	73.07*	1.86	11.7 ± 0.73	22.85	0.269
A6-24(205)	69.93*	0.85	8.2 ± 1.56	23.9	0.512

[a]mass unit indicates grams of iron oxide nanoparticles corrected by TGA.
[b]mass unit indicates milligrams of Fe determined by Prussian blue assay.
[c]Polydispersity Index (PDI) determined by DLS.
*VSM data was corrected using 0.925 percent weight of sample

One interesting finding was that increasing the concentration of $Fe(acac)_3$ actually led to a decrease of crystallite size when the reaction temperature was increased to 205°C, 14.1 ± 0.80 nm to 11.7 ± 0.73 nm to 8.2 ± 1.56 nm. Although the crystallite size decreased, the hydrodynamic diameters remained about the same and the PDI only increased when the concentration of $Fe(acac)_3$ was increased to 6 g. Increasing the temperature will add energy into the system so that generation of monomers, rate of nucleation, and diffusion/reaction rates of growth will all increase. These theorized increases can be seen in **Figure 3.9**. The increase of the polydispersity in reaction A6-24(205) can potentially be explained with the theory of mixed diffusion-reaction growth.[169] Growth is controlled depending on whether growth by diffusion or growth by reaction is the rate limiting step.[169] In the case of A6-24(205) the concentration of Fe is so high that diffusion is very quick and therefore growth is

controlled by how fast the Fe can react with the surface of nuclei which leads to larger size distributions.[169] Additionally, it is thought that the rate of particle growth will be faster than crystalline growth which explains the smaller crystallite size with the same hydrodynamic size, as seen for the reactions A2-24(205), A4-24(205), and A6-24(205). For reactions A2-24(205) and A4-24(205), growth is thought to be limited by diffusion which gives rise to smaller PDI values. Also, at lower concentrations the rate of diffusion will be even slower allowing for more crystalline growth rather than amorphous growth. This explains the larger crystallite sizes for the lower concentrations of reactions at 205°C.

There are two proposed reasons for the trend of decreasing crystallite sizes produced at higher temperature in combination with increased concentration of $Fe(acac)_3$ (A4-24(205) and A6-24(205)). They are rationalized using the LaMer growth models in **Figure 3.9** and **Figure 3.10**. The first rationale, is explained by both temperature and increased concentration increasing the rate of monomer production leading to higher rates of nucleation reached. **Figure 3.9.** schematically depicts this shifting of the LaMer growth model curve based on increasing concentrations of iron precursor. This shifting of peaks to earlier time points corresponds with an increased rate of monomer production to reach the higher concentrations of monomers at earlier time points. Thus with an increased rate of monomer production it is thought that a higher nucleation rate will be reached causing a quicker “burst” nucleation event leading to the same number of nuclei formed, but with growth limited by reaction rather than diffusion. In other words as the concentration is increased the rate of diffusion of monomers will become faster than the rate at which monomers can react and grow on

the as formed nuclei. Due to this it is believed that at some increased concentration the monomers will have less time to grow in a crystalline manner and will grow amorphously. This could be why the reactions A2-24(205), A4-24(205), and A6-24(205) have decreasing crystallite sizes with similar hydrodynamic diameters.

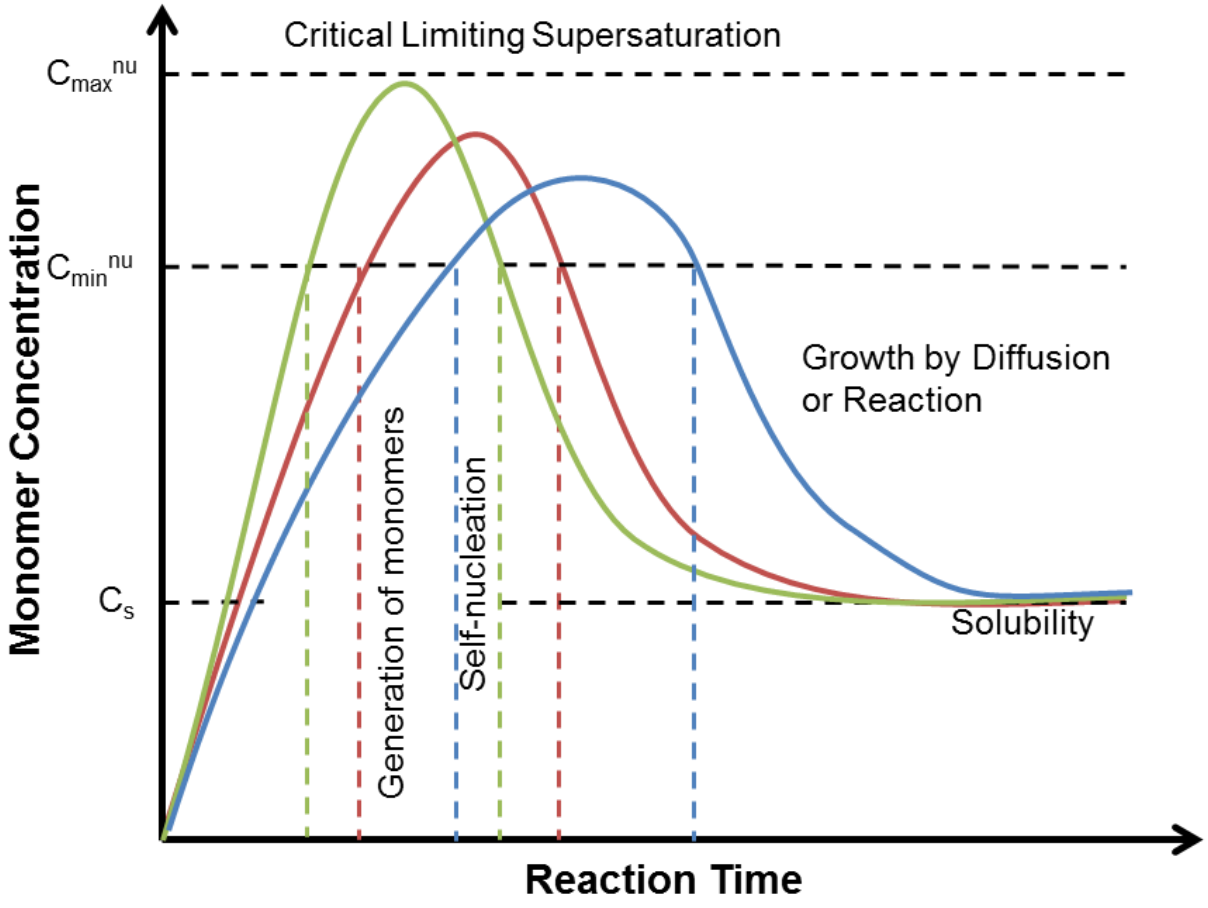

Figure 3.9. Schematic representation of LaMer growth model (blue) depicting the generation of monomers, to formation of nuclei, and growth by diffusion or reaction. The effect of increasing concentration of precursors leading to an increased rate of generation of monomers and longer nucleation time is shown in red and green. Adapted from [166].

The increase in PDI for reaction A6-24(205) may also be explained by the quicker nucleation and a larger difference in rates of growth by diffusion and reaction. In this case, the monomers are overly present in the diffusion layer of the growing nanoparticles. This could lead to monomers diffusing to reaction sites immediately after the previous one reacted and not being able to properly orientate for continued crystal growth. Additionally, the reaction may not have reached the concentration of monomer solubility due to such a high concentration of monomers. Therefore, Ostwald ripening may not have occurred or there was less time for reduction in size distribution by Ostwald ripening.

Another possible explanation for the increased PDI with lower crystallite size and similar hydrodynamic size for the 205°C reactions is that the faster nucleation rates lead to a greater number of smaller nuclei as the concentration is increased. With more nuclei that are initially monodisperse, the growing nanoparticles will then go through Ostwald ripening with one main difference. Ostwald ripening starting with a monodisperse system will lead to a polydisperse system as the nanoparticles will be dissolved to monomers which will then grow on other nanoparticles. This will reduce the number of nanoparticles formed in comparison to the number of nuclei initially formed and thus the PDI will increase. However, the concentration increase from A2-24(205) to A4-24(205) may not be large enough to drastically change the PDI.

An alternative reasoning for the trend of decreasing crystallite sizes produced at higher temperature in combination with increased concentration of $Fe(acac)_3$ (A4-24(205) and A6-24(205)) is thought to be due to a prolonged nucleation stage as well as

higher rates of nucleation reached (**Figure 3.10.**). LaMer growth model suggests that in order for the nucleation stage to end and growth stage to begin, a drop in monomer concentration below the critical supersaturation limit is required.[166,169] In these reactions the higher temperature and concentration of $Fe(acac)_3$ produces monomers faster than they can self-nucleate to deplete the concentration of monomers below the critical limiting supersaturation level (**Figure 3.10.**, green and red curves). This leads to a higher peak where nucleation rates are faster causing more monodisperse nuclei to form before the reaction switches completely to growth. For reaction A4-24(205), this produces more nuclei that are smaller. At this concentration, the growth is switching from limited by diffusion to limited by reaction. This will lead to growth that is more amorphous than crystalline but with similar PDI and hydrodynamic values as compared to A2-24(205). When the concentration of iron precursor is further increased, as in reaction A6-24(205), the peak concentration of monomers is even higher. At this concentration, the limit of production of monomers may have been reached. Production of monomer will continue to occur even at high rates of nucleation leading to longer time required to finish nucleation and switch to growth. This longer nucleation time is schematically represented by peak broadening (**Figure 3.10.** green curve). In other words the increased concentration and prolonged nucleation time decreases the separation of nucleation and growth which leads to higher polydispersity. Additionally, the rate of diffusion is much faster than the rate of reaction leading to even more amorphous growth compared to amount of crystallite growth. Thus resulting in the 8.2 ± 1.56 nm crystallite size and 23.9 nm hydrodynamic size.

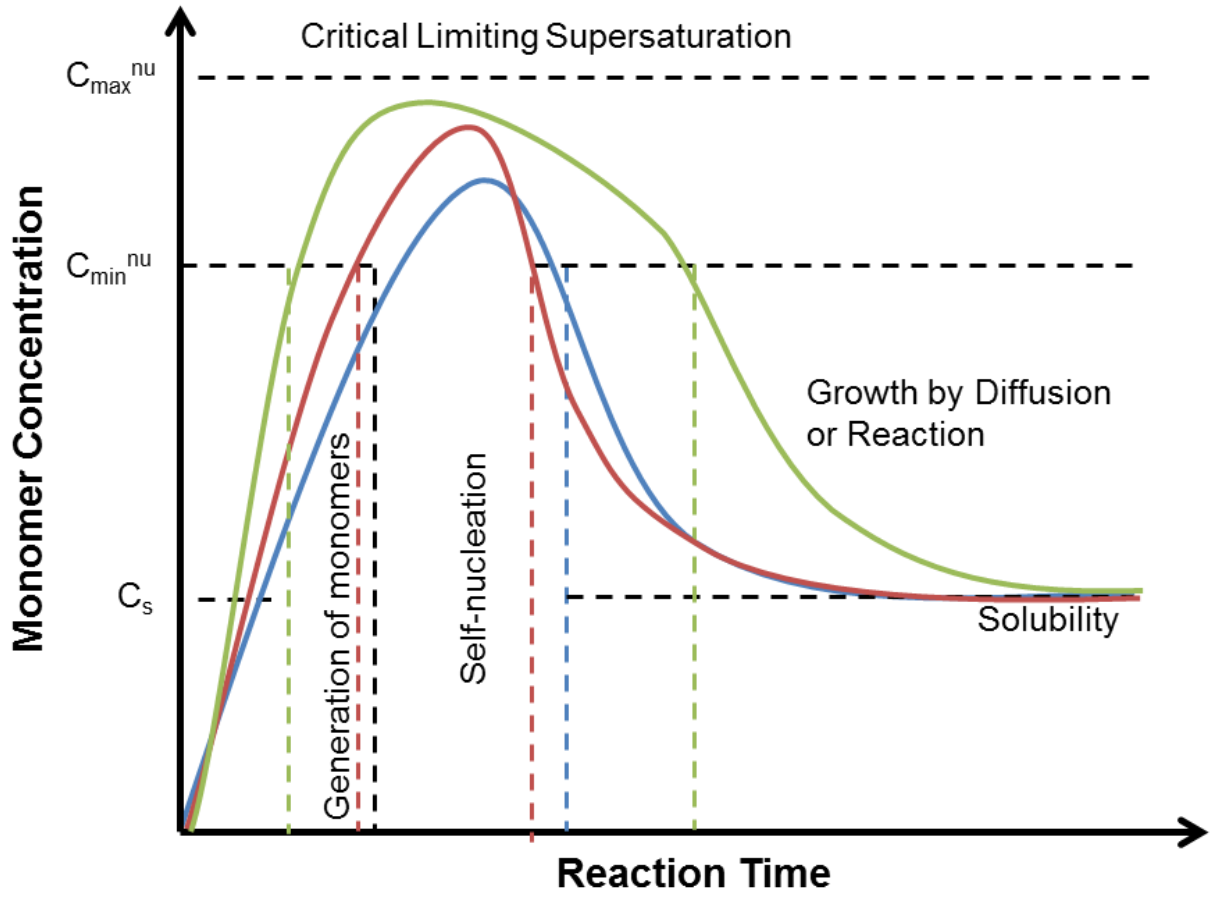

Figure 3.10. Schematic representation of LaMer growth model (blue) depicting the generation of monomers, to formation of nuclei, and growth by diffusion or reaction. The effect of increasing concentration of precursors leading to an increased rate of generation of monomers and longer nucleation time is shown in red and green. Adapted from [166].

From the results of increasing the concentration of $Fe(acac)_3$ it can be concluded that 2 g of $Fe(acac)_3$ is the optimum starting concentration for the benzyl alcohol reaction. The increase in concentration along with increase in temperature to 205°C may have sufficiently shifted the peak in LaMer growth model leading to smaller

crystallite sizes and larger PDI. To further increase the crystallite size while maintaining small PDI values, a modified seed growth procedure was investigated.

3.3.6 Effect of Parameters: Modified Seed Growth

Based on reaction A2-2 the shorter reaction time resulted in a smaller crystallite size. However, the PDI was significantly reduced under these conditions. Thus, it was thought that this level of monodispersity would provide adequate seeds to use in a modified seed growth synthesis to increase the crystallite size further.

The primary difference between traditional seed growth processes and the modification reported here is in the addition step. Traditional methods involve cooling or aging the nanoparticles, followed by washing in organic solvents and drying to a powder to produce the seeds.[95,170,171] These seeds are then redispersed in their solvent and more iron precursor is added before the temperature is increased back to the reaction conditions. In this modified seed growth the addition of more Fe precursor is performed at the "hot" reaction temperatures, and thus the nanoparticles stay dispersed and remain at temperatures suitable for nucleation and growth. Using a second addition with a 2-hour reaction time, A2-2_B2-2, did produce nanoparticles with an increase in overall size (DLS data **Table 3.7**), but this did not increase the crystallite size. As discussed above, the Fe precursor concentration and short reaction time provided lower PDI while the 24 hour step provided a larger crystallite and increased M_S. Therefore, a series of modified seed growth syntheses were conducted with various combinations of $Fe(acac)_3$ concentration and reaction time at the first and second additions (data in **Table 3.7**).

Table 3.7. Nanoparticle characterization of modified seed growth reactions. Saturation Magnetization, Heating Profile, and Average Size determined by VSM, Heating Induction, XRD, and DLS.

Reaction	Magnetization (emu/g)[a]	RF Heating ([°C/min]/mg)[b]	Crystallite size (nm)	Hydrodynamic Diameter (nm)	PDI[c]
A2-24	70.839	0.170	8.8 ± 0.61	13.64	0.703
A2-24(175)	70.91	0.14	8.9 ± 1.39	12.45	0.61
A2-24(195)	74.32	0.18	8.1 ± 0.59	13.3	0.65
A2-24(205)	73.36	2.76	14.1 ± 0.80	24.53	0.275
A2-24_B2-24	75.7	2.536 1.81 ± 0.72†	14.4 ± 2.42 11.8 ± 0.91‡	28.93 24.12 ±4.81†	0.148 0.178±0.03†
A2-24_B2[cool addition]-24	72.488	0.670	9.5 ± 0.71	20.76	0.252
A2-24(175)_B2-24(175)	77.89	1.004	11.6 ± 1.01	24.53	0.404
A2-24(185)_B2-24(185)	77.249	1.068	11.2 ± 0.94	23.11	0.395
A2-24(195)_B2-24(195)	78.202	4.041	14.9 ± 0.74	37.52	0.219
A2-24(205)_B2-24(205)	79.35*	5.55 5.45 ± 0.09†	19.5 ± 1.06 18.05 ±1.91‡	44.63 44.28 ±0.36†	0.265 0.228±0.04†
A2-2	60.6	0.032	5.7 ± 0.76	10.93	0.311
A2-2_B2-2	62.85	0.069	6.5 ± 0.67	17.88	0.447
A2-2_B2-24	76.1	0.211	9.3 ± 0.45	20.07	0.373
A2-2_B4-2	62.8	0.102	9.5 ± 3.46	15.43	0.258
A2-2_B4-24	72.18	0.212	9.8 ± 1.33	17.72	0.304
A2-2_B6-24	75.56	0.639	10.5 ± 1.02	19.42	0.368

[a]mass unit indicates grams of iron oxide nanoparticles corrected by TGA.

[b]mass unit indicates milligrams of Fe determined by Prussian blue assay.

[c]Polydispersity Index (PDI) determined by DLS.

*VSM data was corrected using 0.925 percent weight of sample

Keeping the first addition constant at 2 grams for 2 hours, it was found that a 24-hour step was critical in achieving a larger crystallite size and higher M_s. The sample from this series with the highest crystallite size of 10.5 ± 1.02 nm was A2-2_B6-24. Since this was still under our goal of 15 nm, a seed growth with two 24-hour reaction times was attempted to possibly begin with seeds of larger crystallite size. The “hot”

addition would then allow for continued crystallite growth instead of just particle growth. A2-24_B2-24 not only resulted in an increased crystallite size of 14.4 ± 2.41 nm, but also a decreased PDI of 0.148. To determine reproducibility reaction A2-24_B2-24 was repeated. The averages and standard deviation of the experimental repeats are shown in **Table 3.7**. The crystallite size and PDI have low standard deviations indicating good reproducibility. The hydrodynamic diameter and RF heating values were lower for the experimental repeat leading to larger standard deviations. A representative transmission electron microscopy (TEM) image of A2-24_B2-24 nanoparticles is shown in **Figure 3.11**. This increase in monodispersity is speculated to be due to the "hot" addition, providing an initial burst nucleation of small nuclei which are subsequently dissolved and grow on the larger seeds already present in solution in agreement with "Ostwald ripening".[172,173] Additionally this mechanism of growth can increase the monodispersity of nanoparticles formed.[174] To corroborate this "hot" addition mechanism, a similar reaction was cooled to 30°C before the second addition of iron precursor, A2-24_B2(30)-24. This resulted in nanoparticles with a smaller crystallite size of 9.5 ± 0.71 nm and an increased PDI of 0.252, which suggests that the "hot" addition does indeed facilitate the continued crystallite growth and is an important parameter of this synthesis.

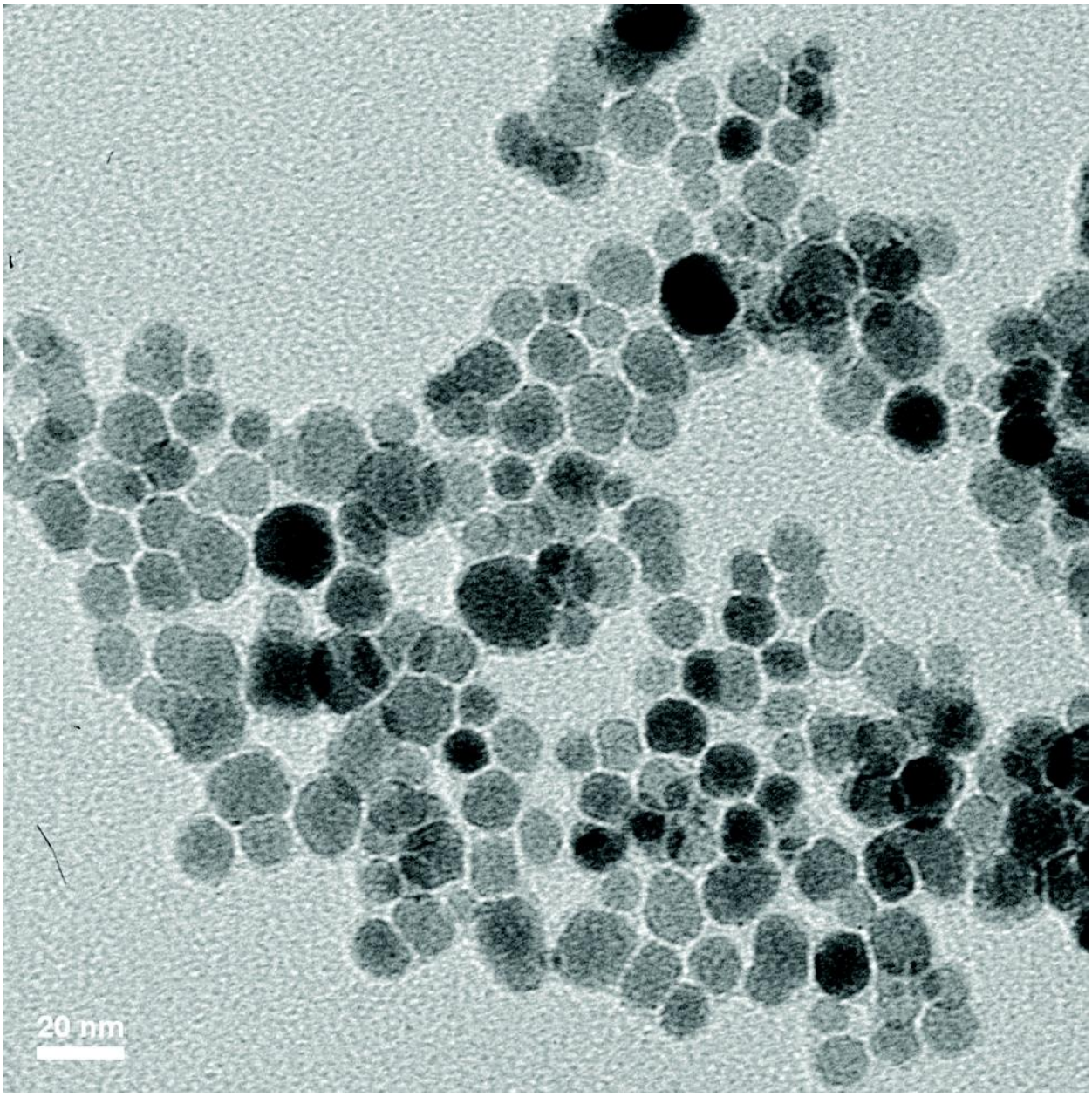

Figure 3.11. TEM images of iron oxide nanoparticles synthesized in air by the modified seed growth, A2-24_B2-24, and dispersed with TMAOH. Particle diameters are 15.28 ± 2.21 nm, as determined using Image J software.

The next parameter investigated for modified seed growth parameters was reaction temperature. Using a silicone oil bath for precise temperature control, the

reaction temperature was varied for the modified seed growth reactions A2-24(175)_B2-24(175), A2-24(185)_B2-24(185), A2-24(195)_B2-24(195), and A2-24(205)_B2-24(205) (**Table 3.7.**). A2-24(175)_B2-24(175) resulted in a crystallite size of 11.6 ± 1.01 nm with a PDI of 0.404. Raising the temperature to 185°C, 195°C, and 205°C was hypothesized to increase the crystallite size and lower the PDI by promoting the Oswald ripening process and providing better separation of nucleation and growth. Indeed, the crystallite size increased to 13.2 nm for A2-24(185)_B2-24(185), to 15.2 nm for A2-24(195)_B2-24(195), and further increased to 19.5 ± 1.06 nm for A2-24(205)_B2-24(205). The 195°C reaction yielded the lowest PDI of 0.219 for the temperature series with two additions of 2 grams of $Fe(acac)_3$. The second addition of iron precursor most likely facilitated additional Ostwald ripening to focus the size distribution of nanoparticles produced from the first addition as evidenced by the lower PDI in the modified seed growth for their respective temperatures. The reaction at 205°C yielded the highest crystallite and hydrodynamic diameter with a relatively low PDI value, but had the highest RF heating value of all reactions investigated. This was unexpected as the RF heating capabilities should exponentially decrease as the crystallite size is increased above the desired 15 nm. It is possible that these nanoparticles have a larger volume percentage of nanoparticles that are closer to the desired 15 nm crystallite size, since XRD is biased towards larger crystallite sizes. An experimental repeat of reaction A2-24(205)_B2-24(205) was conducted to determine reproducibility. The characterization averages and standard deviations for the experimental repeat are shown in **Table 3.7**. The standard deviations for all of the characterizations indicate high reproducibility. In addition the lower crystallite size of the experimental repeat indicates that the 19.5 ±

1.06 nm crystallite size was most likely due to XRD measurement bias towards larger crystallite sizes. This is corroborated by the fact that all of the characterizations except for the crystallite size had very low standard deviations for the experimental repeat. The SAR value for reaction A2-24(205)_B2-24(205) was estimated to be 1,175.56 $\frac{W}{g}$ using the specific heat of water c_{H2O} = 4.18 $\frac{Ws}{gK}$ as a close approximation of the true specific heat. The SAR of 1,175.56 $\frac{W}{g}$ was then used with the H = 37.4 $\frac{kA}{m}$ and f = 270 kHz to determine the ILP = 3.1127 $\frac{nHm^2}{kg}$. While these nanoparticles are not surface functionalized their approximate ILP values are comparable to some of the highest commercially available synthetic ferrofluids (ILP = 0.15-3.12 $\frac{nHm^2}{kg}$).[21] Interestingly, the temperature effect on crystallite size was not as clearly defined when running only one 24-hour reaction with samples A2-24(175), A2-24(195), and A2-24(205). The crystallite sizes initially decreased from 9.1 nm to 7.8 nm for A2-24(175) and A2-24(195) respectively, and then increased to 14.1 nm in reaction A2-24(205) (**Table 3.5**).

Since A2-24(205)_B2-24(205) produced nanoparticles with the largest RF heating capabilities, larger first and second additions of $Fe(acac)_3$ were investigated in an attempt to lower the PDI while retaining the same crystallite size. These reactions are shown in **Table 3.8**.

Table 3.8. Nanoparticle characterization of modified seed growth reactions with varying concentrations at first and second additions. Saturation Magnetization, Heating Profile, and Average Size determined by VSM, Heating Induction, XRD, and DLS.

Reaction	Magnetization (emu/g)[a]	RF Heating ([°C/min]/mg)[b]	Crystallite size (nm)	Hydrodynamic Diameter (nm)	PDI[c]
A2-24(195)_B2-24(195)	78.202	4.04	14.9 ± 0.74	37.52	0.219
A2-24(205)_B2-24(205)	79.35*	5.55 5.45 ± 0.09†	19.5 ± 1.06 18.05 ±1.91‡	44.63 44.28 ±0.36†	0.265 0.228±0.04†
A4-24(195)_B2-24(195)	75.12*	3.13	14.95 ± 2.03	29.5	0.36
A4-24(195)_B4-24(195)	76.56*	4.48	13.4 ±1.61	31.94	0.121
A4-24(205)_B4-24(205)		2.74	12.4 ± 1.11	26.67	0.146
A4-24(195)_B6-24(195)	76.99*	3.43	15.2 ± 1.50	26.6	0.112
A4-24(205)_B6-24(205)	85.26*	3.14	15.3 ± 2.45	28.2	0.14
A6-24(195)_B2-24(195)	71.64*	2.71	11.4 ± 1.25	43.89	0.305
A6-24(195)_B4-24(195)	72.74*	2.88	12.9 ± 0.92	23.5	0.176
A6-24(195)_B6-24(195)	75.1*	2.58	14.1 ±0.98	26.19	0.231

[a]mass unit indicates grams of iron oxide nanoparticles corrected by TGA.
[b]mass unit indicates milligrams of Fe determined by Prussian blue assay.
[c]Polydispersity Index (PDI) determined by DLS.
*VSM data was corrected using 0.925 percent weight of sample

The reaction A4-24(195)_B2-24(195) produces a crystallite size of 14.95 ± 2.03 nm and PDI of 0.36 which explains the decrease in RF heating. The concentration of the second addition is vital as the newly formed monomers can either form new nuclei or grow on the seeds present. The new nuclei are rapidly dissolved into the solution as monomers and grow on the seeds in accordance with Ostwald ripening.[172,173] With only 2 g of second addition the new monomers may only grow on a fraction of the seeds which leads to larger size distribution. The larger crystallite size can also be explained by Ostwald ripening where it is energetically more favorable for the monomers to grow on the larger nanoparticles. At sufficiently high concentrations of monomers all of the seeds will have an approximately equal number of monomers in its respective diffusion

layer.[175] In this case all seeds will grow instead of smaller seeds being dissolved to form monomers for growth on the larger seeds. This process reduces the surface energy and is therefore energetically favored.[176] Since all seeds are growing and smaller seeds will have a faster growth rate, the smaller seeds will "catch up" to the size of the larger sized seeds.[175] In other words, more monomers are required for larger nanoparticles to grow by the same amount, in terms of increase of diameter increase, than smaller nanoparticles.[175] Thus reducing the size distribution as evidenced in the lower PDI and also increasing the crystallite size for reactions A4-24(195)_B4-24(195), A4-24(195)_B6-24(195), A6-24(195)_B4-24(195), and A6-24(195)_B6-24(195).

The smaller crystallite size of 11.4 ± 1.25 nm in reaction A6-24(195)_A2-24(195) is most likely due to starting with a smaller crystallite size after the first addition as evidenced by the crystallite size of 9.3 nm for reaction A6-24(195). Then following the idea that the monomer concentration was insufficiently high at the second addition to saturate the diffusion layer of each seed, the smaller seeds will be dissolved for growth and reducing the PDI in accordance with Ostwald ripening. Therefore, for these reactions a second addition of 4 or 6 g of iron precursor is necessary for larger crystallite growth with low size distribution.

3.3.7 Examination of Radiofrequency Induced Heating Properties

Compiling all of the data in **Table 3.9**, there are several conclusions to be drawn from the relationship between RF heating rate, particle characteristics, and synthetic parameters.

Table 3.9. Nanoparticle characterization of all reactions. Saturation Magnetization, Heating Profile, and Average Size determined by VSM, Heating Induction, XRD, and DLS for reactions carried out under nitrogen (blue), air for 24 hours (green) and air for less than 6 hours (red).

Reaction	Magnetization (emu/g)[a]	RF Heating ([°C/min]/mg)[b]	Crystallite size (nm)	Hydrodynamic Diameter (nm)	PDI[c]
N_2-A2-24	53.39		6.47 ± 1.17	23.23	0.351
N_2-A2-24(150)	48.54*	0.01	5.65 ± 0.76	13.02	0.372
N_2-A2-24(175)	57.69	0.04	6.06 ± 0.52	11.51	0.306
N_2-A2-24(195)	57.09*	0.02	6.3 ± 0.89		
N_2-A2-24(205)	57.56*	0.05	11.3 ± 0.73	38.48	0.152
A2-24	70.839	0.170	8.8 ±0.61	13.64	0.703
A2-24(125)	-	-	-	-	-
A2-24(150)	55.50	0.06	6.2	13.58	0.589
A2-24(175)	70.91	0.142	8.9 ±1.39	12.45	0.61
A2-24(195)	74.322	0.175	8.1 ± 0.59	13.3	0.65
A4-24	68.99	0.134	8.3	14.68	0.2
A6-24	68.25	0.219	7.9	16.5	0.164
A2-24(205)	73.36*	2.76	14.1 ± 0.80	24.53	0.275
A4-24(205)	73.07*	1.86	11.7 ± 0.73	22.85	0.269
A6-24(205)	69.93*	0.85	8.2 ± 1.56	23.9	0.512
A2-24_B2-24	75.7	2.536 1.81 ± 0.72†	14.4 ± 2.42 11.8 ± 0.91‡	28.93 24.12 ±4.81†	0.148 0.178±0.03†
A2-24_B2[cool addition]-24	72.488	0.670	9.5 ± 0.71	20.76	0.252
A2-24(175)_B2-24(175)	77.89	1.004	11.6 ± 1.01	24.53	0.404
A2-24(185)_B2-24(185)	77.249	1.068	11.2 ± 0.94	23.11	0.395
A2-24(195)_B2-24(195)	78.202	4.041	14.9 ± 0.74	37.52	0.219
A2-24(205)_B2-24(205)	79.35*	5.55 5.45 ± 0.09†	19.5 ± 1.06 18.05 ±1.91‡	44.63 44.28 ±0.36†	0.265 0.228±0.04†
A4-24(195)_B2-24(195)	75.12*	3.13	14.95 ± 2.03	29.5	0.36
A4-24(195)_B4-24(195)	76.56*	4.48	13.4 ±1.61	31.94	0.121
A4-24(205)_B4-24(205)		2.74	12.4 ± 1.11	26.67	0.146
A4-24(195)_B6-24(195)	76.99*	3.43	15.2 ± 1.50	26.6	0.112
A4-24(205)_B6-24(205)	85.26*	3.14	15.3 ± 2.45	28.2	0.14
A6-24(195)_B2-24(195)	71.64*	2.71	11.4 ± 1.25	43.89	0.305
A6-24(195)_B4-24(195)	72.74*	2.88	12.9 ± 0.92	23.5	0.176
A6-24(195)_B6-24(195)	75.1*	2.58	14.1 ±0.98	26.19	0.231
A2-2	60.6	0.032	5.7 ± 0.76	10.93	0.311
A2-2_B2-2	62.85	0.069	6.5 ± 0.67	17.88	0.447
A2-2_B2-2_C2-2	65.1	0.06	7.4	17.82	0.258
A2-2_B2-24	76.1	0.211	9.3 ± 0.45	20.07	0.373
A2-2_B4-2	62.8	0.102	9.5 ± 3.46	15.43	0.258
A2-2_B4-24	72.18	0.212	9.8 ± 1.33	17.72	0.304
A2-2_B6-24	75.56	0.639	10.5 ± 1.02	19.42	0.368

[a]mass unit indicates grams of iron oxide nanoparticles corrected by TGA.

[b]mass unit indicates milligrams of Fe determined by Prussian blue assay.
[c]Polydispersity Index (PDI) determined by DLS.
*VSM data was corrected using 0.925 and 0.88 percent weight of samples in air and under nitrogen respectively
[†]Average with standard deviation of experimental repeat
[‡]Average crystallite size determined by one peak with standard deviation of experimental repeat

First, nanoparticles produced without a 24 hour reaction step all resulted in M_s values between 60-65 emu/g as shown in **Figure 3.12A,C,E** (red squares). Upon incorporating a 24 hour step, whether at each addition or only the second addition (e.g. – A2-2_B2-24), the M_s increased to 72-78 emu/g (**Figure 3.12A,C,E** – green triangles). While the M_s also showed a positive correlation with crystallite size (**Figure 3.12A**) and hydrodynamic diameter (**Figure 3.12C**), there was not a clear correlation between RF heating and M_s (**Figure 3.12E**).

Next, in agreement with the literature, there was a strong correlation between RF heating and crystallite size with a sharp increase as the crystallite size approaches 15 nm and a sharp decrease as crystallite size is increased beyond 15 nm (**Figure 3.12B**). The data also shows a correlation between the RF heating and hydrodynamic diameter (**Figure 3.12D**). While this could be primarily due to the linear correlation between crystallite size and hydrodynamic diameter (**Figure 3.13B**), it could also suggest that there is an optimal hydrodynamic diameter to provide maximal heat exchange between the particle and the surrounding environment. There is no clear correlation between crystallite size and PDI (**Figure 3.13A)**. Further studies will be needed to determine this contribution. Lastly, there is an overall negative correlation between RF heating and PDI, which indicates a system that is more monodispersed has improved heating. However, particle size (both crystallite and hydrodynamic diameter) and size distribution

appear to be the dominant determining factors in optimal RF heating for iron oxide nanoparticles

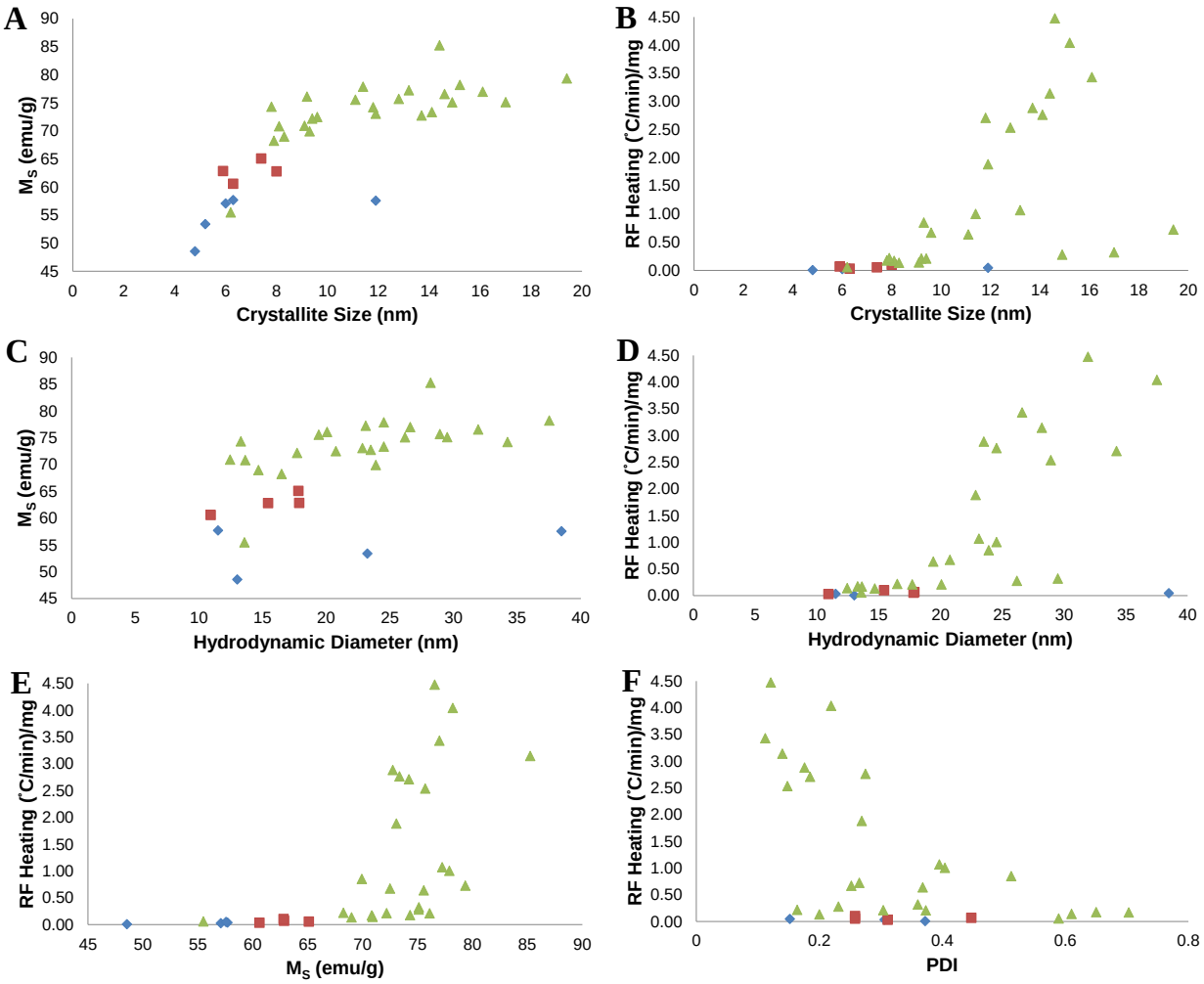

Figure 3.12. Comparison of syntheses conducted under nitrogen flow (blue), open to air with total reaction times less than 6 hours (red), and open to air with reactions involving at least one 24 hour reaction step (green). (A, B) Plots of crystallite size versus M_s and RF heating. (C, D) Plots of hydrodynamic diameter versus M_s and RF heating. (E) Plot showing M_s versus RF heating. (F) Plot of polydispersity index versus RF heating.

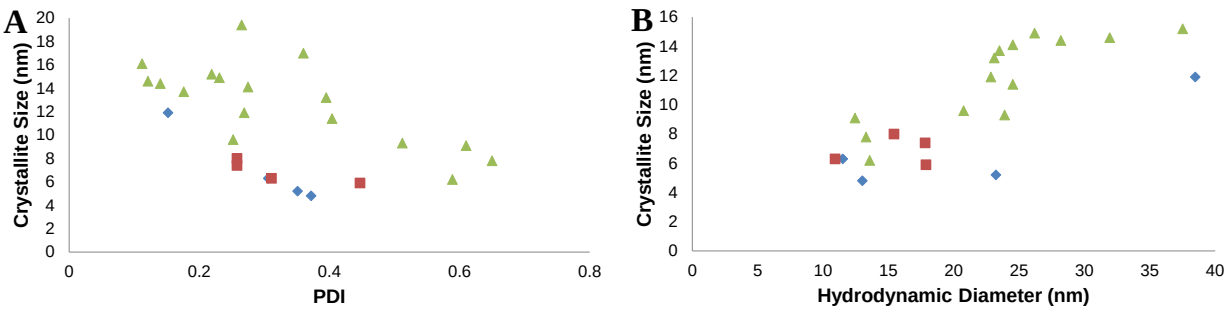

Figure 3.13. Plot of PDI versus crystallite size (A) and hydrodynamic diameter versus crystallite size (B), comparing syntheses conducted under nitrogen flow (blue), under atmospheric conditions with total reaction times less than 6 hours (red), and under atmospheric conditions with reactions involving at least one 24 hour reaction step (green).

3.4 Conclusion

The goal of this thesis was to develop and optimize a modified seed growth of iron oxide nanoparticles in benzyl alcohol specific for radiofrequency induced heating of magnetic nanoparticle colloidal solutions for hyperthermia cancer therapy. To accomplish this goal the effects of changing synthetic parameters such as reaction environment, time, temperature and concentration were investigated. The main conclusions of this thesis are included below.

1. Carrying out the benzyl alcohol synthesis open to air, rather than under nitrogen flow, allowed an additional mechanism of monomer production for a larger separation of nucleation and growth. It is thought that oxidation of benzyl alcohol

to benzaldehyde and reduction of $Fe(acac)_3$ occurs giving rise to a larger separation of nucleation and growth producing larger crystallite sizes. This is evidenced by refluxing beginning just above the boiling point of benzaldehyde (178.1°C). Further verification of an additional mechanism was obtained by running the reaction similar to glycol methods.

2. It is hypothesized that the oxidation-reduction mechanisms gives rise to more magnetite and thus higher magnetization saturation values observed for reactions carried out open to air. Further studies are needed to confirm this.
3. It was found that longer time lengths in combination with higher temperatures and concentrations produced crystallites sizes close to the desired 15 nm with relatively low size distribution. The modified seed growth allowed for even larger crystallite sizes and better radiofrequency heating rates.
4. Increasing the reaction temperature and/or concentration gives rise to larger separation of nucleation and growth via a “burst” nucleation event. A “burst” nucleation event results in larger crystallite sizes and smaller size distributions. It is thought that increasing the temperature or concentration of iron precursor the rate of production of monomers increases and higher rates of nucleation are reached. This can lead to either a quicker “burst” nucleation or a prolonged nucleation event depending on the concentration of iron precursor available and the rate of monomer production. These two scenarios in combination with mixed diffusion-reaction growth and Ostwald ripening explains the range of crystallite size and polydispersion indexes observed. It was found that at some point increasing the concentration and temperature further leads to more unwanted

amorphous growth, smaller crystallite size, and a wider size distribution. Thus, by controlling the concentration and reaction temperature, the best RF heating properties were obtained for nanoparticles synthesized by reaction A2-24(205)_B2-24(205). The estimated SAR of 1,175.56 W/g and ILP value of 3.113 $\frac{nHm^2}{kg}$ for these nanoparticles are consistent with commercially available ferrofluids.[21] These nanoparticle had a crystallite size of 14.6 nm and PDI of 0.121. The trends observed for nanoparticle characteristics effect on radiofrequency heating are in agreement with the literature.

This investigation of synthesis parameters has provided a better understanding of the mechanism of nucleation and growth in the benzyl alcohol synthesis of iron oxide nanoparticles. Utilizing the modified seed growth allowed for optimization and control over resultant nanoparticle characteristics and radiofrequency induced magnetic heating properties. These nanoparticles could be widely beneficial for magnetic hyperthermia treatment of cancer.

References

References

1. Gilchrist, R. K.; Medal, R.; Shorey, W. D.; Hanselman, R. C.; Parrott, J. C.; Taylor, C. B. Selective Inductive Heating of Lymph Nodes. *Ann. Surg.* **1957***, 146*.

2. Gazeau, F.; Levy, M.; Wilhelm, C. Optimizing magnetic nanoparticle design for nanothermotherapy. *Nanomedicine* **2008***, 3*, 831-844.

3. Song, C.; Park, H.; Griffin, R. Improvement of tumor oxygenation by mild hyperthermia. *Radiat. Res.* **2001***, 155*, 515-528.

4. Peer, A. J.; Grimm, M. J.; Zynda, E. R.; Repasky, E. A. Diverse immune mechanisms may contribute to the survival benefit seen in cancer patients receiving hyperthermia. *Immunol. Res.* **2010***, 46*, 137-154.

5. Spiro, I.; McPherson, S.; Cook, J.; Ling, C.; Degraff, W.; Mitchell, J. Sensitization of Low-Dose-Rate Irradiation by Nonlethal Hyperthermia. *Radiat. Res.* **1991***, 127*, 111-114.

6. Kumar, C. S. S. R.; Mohammad, F. Magnetic nanomaterials for hyperthermia-based therapy and controlled drug delivery. *Adv. Drug Deliv. Rev.* **2011***, 63*, 789-808.

7. Goldstein, L.; Dewhirst, M.; Repacholi, M.; Kheifets, L. Summary, conclusions and recommendations: adverse temperature levels in the human body. *International Journal of Hyperthermia* **2003***, 19*, 373-384.

8. Beachy, S. H.; Repasky, E. A. Toward establishment of temperature thresholds for immunological impact of heat exposure in humans. *International Journal of Hyperthermia* **2011***, 27*, 344-352.

9. Krishnan, S.; Diagaradjane, P.; Cho, S. H. Nanoparticle-mediated thermal therapy: Evolving strategies for prostate cancer therapy. *International Journal of Hyperthermia* **2010***, 26*, 775-789.

10. Mornet, S.; Vasseur, S.; Grasset, F.; Duguet, E. Magnetic nanoparticle design for medical diagnosis and therapy. *Journal of Materials Chemistry* **2004***, 14*, 2161-2175.

11. Jordan, A.; Scholz, R.; Wust, P.; Fahling, H.; Felix, R. Magnetic fluid hyperthermia (MFH): Cancer treatment with AC magnetic field induced excitation of biocompatible superparamagnetic nanoparticles. *J Magn Magn Mater* **1999***, 201*, 413-419.

12. van der Zee, J. Heating the patient: a promising approach? *Annals of Oncology* **2002***, 13*, 1173-1184.

13. Reinhold, H. S.; Endrich, B. Tumour microcirculation as a target for hyperthermia. *Int. J. Hyperthermia* **1986***, 2*, 111-137.

14. Jordan, A.; Wust, P.; Fahling, H.; John, W.; Hinz, A.; Felix, R. Inductive Heating of Ferrimagnetic Particles and Magnetic Fluids - Physical Evaluation of their Potential for Hyperthermia. *International Journal of Hyperthermia* **1993***, 9*, 51-68.

15. Rosensweig, R. Heating magnetic fluid with alternating magnetic field. *J Magn Magn Mater* **2002***, 252*, 370-374.

16. Ma, M.; Wu, Y.; Zhou, H.; Sun, Y.; Zhang, Y.; Gu, N. Size dependence of specific power absorption of Fe3O4 particles in AC magnetic field. *J Magn Magn Mater* **2004***, 268*, 33-39.

17. Lee, J.; Jang, J.; Choi, J.; Moon, S. H.; Noh, S.; Kim, J.; Kim, J.; Kim, I.; Park, K. I.; Cheon, J. Exchange-coupled magnetic nanoparticles for efficient heat induction. *Nature Nanotechnology* **2011***, 6*, 418-422.

18. Rochmann, P. Radiofrequency Penetraion and Absorption in the Human Body – Limitations to High-Field Whole-Body Nuclear-Magnetic-Resonance Imaging. *Med. Phys.* **1987**, 14, 922-931.

19. Hergt, R.; Dutz, S. Magnetic particle hyperthermia—biophysical limitations of a visionary tumour therapy. *J Magn Magn Mater* **2007***, 311*, 187-192.

20. Singh, D.; McMillan, J. M.; Kabanov, A. V.; Sokolsky-Papkov, M.; Gendelman, H. E. Bench-to-bedside translation of magnetic nanoparticles. *Nanomedicine* **2014***, 9*, 501-516.

21. Kallumadil, M.; Tada, M.; Nakagawa, T.; Abe, M.; Southern, P.; Pankhurst, Q. A. Suitability of commercial colloids for magnetic hyperthermia. *J Magn Magn Mater* **2009***, 321*, 1509-1513.

22. Torres-Lugo, M.; Rinaldi, C. Thermal potentiation of chemotherapy by magnetic nanoparticles. *Nanomedicine* **2013***, 8*, 1689-1707.

23. Laurent, S.; Forge, D.; Port, M.; Roch, A.; Robic, C.; Elst, L. V.; Muller, R. N. Magnetic iron oxide nanoparticles: Synthesis, stabilization, vectorization, physicochemical characterizations, and biological applications. *Chem. Rev.* **2008***, 108*, 2064-2110.

24. Jeyadevan, B. Present status and prospects of magnetite nanoparticles-based hyperthermia. *Journal of the Ceramic Society of Japan* **2010***, 118*, 391-401.

25. Issa, B.; Obaidat, I. M.; Albiss, B. A.; Haik, Y. Magnetic Nanoparticles: Surface Effects and Properties Related to Biomedicine Applications. *International Journal of Molecular Sciences* **2013***, 14*, 21266-21305.

26. Brown, W. F. Thermal Fluctuations of a Single-Domain Particle. *J. Appl. Phys.* **1963***, 34*, 1319-1320.

27. Brown, W. F. Thermal Fluctuations of a Single-Domain Particle. *Phys. Rev.* **1963***, 130*, 1677-1686.

28. Hanson, M. The Frequency-Dependence of the Complex Susceptibility of Magnetic Liquids. *J Magn Magn Mater* **1991***, 96*, 105-113.

29. Shliomis, M. I.; Pshenichnikov, A. F.; Morozov, K. I.; Shurubor, I. Y. Magnetic properties of ferrocolloids. *J Magn Magn Mater* **1990***, 85*, 40-46.

30. Deatsch, A. E.; Evans, B. A. Heating efficiency in magnetic nanoparticle hyperthermia. *J Magn Magn Mater* **2014***, 354*, 163-172.

31. Huang, S.; Wang, S.; Gupta, A.; Borca-Tasciuc, D.; Salon, S. J. On the measurement technique for specific absorption rate of nanoparticles in an alternating electromagnetic field. *Meas Sci Technol* **2012***, 23*, 035701.

32. Suto, M.; Hirota, Y.; Mamiya, H.; Fujita, A.; Kasuya, R.; Tohji, K.; Jeyadevan, B. Heat dissipation mechanism of magnetite nanoparticles in magnetic fluid hyperthermia. *J Magn Magn Mater* **2009***, 321*, 1493-1496.

33. Lemine, O. M.; Omri, K.; Iglesias, M.; Velasco, V.; Crespo, P.; de la Presa, P.; El Mir, L.; Bouzid, H.; Yousif, A.; Al-Hajry, A. gamma-Fe2O3 by sol-gel with large nanoparticles size for magnetic hyperthermia application. *J. Alloys Compounds* **2014***, 607*, 125-131.

34. Yuan, Y.; Tasciuc, D. B. Comparison between experimental and predicted specific absorption rate of functionalized iron oxide nanoparticle suspensions. *J Magn Magn Mater* **2011***, 323*, 2463-2469.

35. Hergt, R.; Dutz, S.; Mueller, R.; Zeisberger, M. Magnetic particle hyperthermia: nanoparticle magnetism and materials development for cancer therapy. *Journal of Physics-Condensed Matter* **2006***, 18*, S2919-S2934.

36. Karimi, Z.; Karimi, L.; Shokrollahi, H. Nano-magnetic particles used in biomedicine: Core and coating materials. *Materials Science & Engineering C-Materials for Biological Applications* **2013***, 33*, 2465-2475.

37. Shenoi, M. M.; Shah, N. B.; Griffin, R. J.; Vercellotti, G. M.; Bischof, J. C. Nanoparticle preconditioning for enhanced thermal therapies in cancer. *Nanomedicine* **2011***, 6*, 545-563.

38. Fillmore, H. L.; Shultz, M. D.; Henderson, S. C.; Cooper, P.; Broaddus, W. C.; Chen, Z. J.; Shu, C.; Zhang, J.; Ge, J.; Dorn, H. C.; Corwin, F.; Hirsch, J. I.; Wilson, J.; Fatouros, P. P. Conjugation of functionalized gadolinium metallofullerenes with IL-13 peptides for targeting and imaging glial tumors. *Nanomedicine* **2011***, 6*, 449-458.

39. Hergt, R.; Hiergeist, R.; Hilger, I.; Kaiser, W.; Lapatnikov, Y.; Margel, S.; Richter, U. Maghemite nanoparticles with very high AC-losses for application in RF-magnetic hyperthermia. *J Magn Magn Mater* **2004***, 270*, 345-357.

40. Creixell, M.; Bohorquez, A. C.; Torres-Lugo, M.; Rinaldi, C. EGFR-Targeted Magnetic Nanoparticle Heaters Kill Cancer Cells without a Perceptible Temperature Rise. *Acs Nano* **2011***, 5*, 7124-7129.

41. Domenech, M.; Marrero-Berrios, I.; Torres-Lugo, M.; Rinaldi, C. Lysosomal Membrane Permeabilization by Targeted Magnetic Nanoparticles in Alternating Magnetic Fields. *Acs Nano* **2013***, 7*, 5091-5101.

42. Sun, C.; Lee, J. S. H.; Zhang, M. Magnetic nanoparticles in MR imaging and drug delivery. *Adv. Drug Deliv. Rev.* **2008***, 60*, 1252-1265.

43. Weissleder, R.; Stark, D.; Engelstad, B.; Bacon, B.; Compton, C.; White, D.; Jacobs, P.; Lewis, J. Superparamagnetic Iron-Oxide - Pharmacokinetics and Toxicity. *Am. J. Roentgenol.* **1989***, 152*, 167-173.

44. Shultz, M. D.; Wilson, J. D.; Fuller, C. E.; Zhang, J.; Dorn, H. C.; Fatouros, P. P. Metallofullerene-based Nanoplatform for Brain Tumor Brachytherapy and Longitudinal Imaging in a Murine Orthotopic Xenograft Model. *Radiology* **2011***, 261*, 136-143.

45. Wilson, J. D.; Broaddus, W. C.; Dorn, H. C.; Fatouros, P. P.; Chalfant, C. E.; Shultz, M. D. Metallofullerene-Nanoplatform-Delivered Interstitial Brachytherapy Improved Survival in a Murine Model of Glioblastoma Multiforme. *Bioconjug. Chem.* **2012***, 23*, 1873-1880.

46. Fatouros, P. P.; Shultz, M. D. Metallofullerenes: a new class of MRI agents and more? *Nanomedicine* **2013***, 8*, 1853-1864.

47. Kelkar, S. S.; Reineke, T. M. Theranostics: Combining Imaging and Therapy. *Bioconjug. Chem.* **2011***, 22*, 1879-1903.

48. Carroll, K. J.; Shultz, M. D.; Fatouros, P. P.; Carpenter, E. E. High magnetization aqueous ferrofluid: A simple one-pot synthesis. *J. Appl. Phys.* **2010***, 107*, 09B304.

49. Gupta, A.; Gupta, M. Synthesis and surface engineering of iron oxide nanoparticles for biomedical applications. *Biomaterials* **2005***, 26*, 3995-4021.

50. Johannsen, M.; Gneveckow, U.; Taymoorian, K.; Thiesen, B.; Waldoefner, N.; Scholz, R.; Jung, K.; Jordan, A.; Wust, P.; Loening, S. A. Morbidity and quality of life during thermotherapy using magnetic nanoparticles in locally recurrent prostate cancer: Results of a prospective phase I trial. *International Journal of Hyperthermia* **2007***, 23*, 315-323.

51. Singh, A.; Patel, T.; Hertel, J.; Bernardo, M.; Kausz, A.; Brenner, L. Safety of Ferumoxytol in Patients With Anemia and CKD. *American Journal of Kidney Diseases* **2008***, 52*, 907-915.

52. Auerbach, M. Ferumoxytol as a New, Safer, Easier-to-Ad minister Intravenous Iron: Yes or No? *American Journal of Kidney Diseases* **2008***, 52*, 826-829.

53. Spinowitz, B. S.; Kausz, A. T.; Baptista, J.; Noble, S. D.; Sothinathan, R.; Bernardo, M. V.; Brenner, L.; Pereira, B. J. G. Ferumoxytol for Treating Iron Deficiency Anemia in CKD. *Journal of the American Society of Nephrology* **2008***, 19*, 1599-1605.

54. Reimer, P.; Balzer, T. Ferucarbotran (Resovist): a new clinically approved RES-specific contrast agent for contrast-enhanced MRI of the liver: properties, clinical development, and applications. *Eur. Radiol.* **2003***, 13*, 1266-1276.

55. Maier-Hauff, K.; Rothe, R.; Scholz, R.; Gneveckow, U.; Wust, P.; Thiesen, B.; Feussner, A.; von Deimling, A.; Waldoefner, N.; Felix, R.; Jordan, A. Intracranial thermotherapy using magnetic nanoparticles combined with external beam radiotherapy: Results of a feasibility study on patients with glioblastoma multiforme. *J. Neurooncol.* **2007***, 81*, 53-60.

56. Pradhan, P.; Giri, J.; Samanta, G.; Sarma, H. D.; Mishra, K. P.; Bellare, J.; Banerjee, R.; Bahadur, D. Comparative evaluation of heating ability and biocompatibility of different ferrite-based magnetic fluids for hyperthermia application. *Journal of Biomedical Materials Research Part B-Applied Biomaterials* **2007***, 81B*, 12-22.

57. Pennacchioli, E.; Fiore, M.; Gronchi, A. Hyperthermia as an adjunctive treatment for soft-tissue sarcoma. *Expert Review of Anticancer Therapy* **2009***, 9*, 199-210.

58. Maeda, H. The enhanced permeability and retention (EPR) effect in tumor vasculature: The key role of tumor-selective macromolecular drug targeting. *Advances in Enzyme Regulation, Vol 41* **2001***, 41*, 189-207.

59. Rishton, S.; Lu, Y.; Altman, R.; Marley, A.; Bian, X.; Jahnes, C.; Viswanathan, R.; Xiao, G.; Gallagher, W.; Parkin, S. Magnetic tunnel junctions fabricated at tenth-

micron dimensions by electron beam lithography. *Microelectronic Engineering* **1997***, 35*, 249-252.

60. Nasu, T.; Tokumitsu, K.; Konno, T.; Suzuki, K. Reduction of iron-oxide by ball-milling with hydrogen gas flow. *Metastable, Mechanically Alloyed and Nanocrystalline Materials, Pts 1 and 2* **2000***, 343-3*, 435-440.

61. Tokumitsu, K.; Nasu, T.; Suzuki, K.; Greer, A. Deoxidation of iron oxide by ball-milling. *Mechanically Alloyed, Metastable and Nanocrystalline Materials, Part 1* **1998***, 269-2*, 181-186.

62. Suryanarayana, C. Mechanical alloying and milling. *Progress in Materials Science* **2001***, 46*, 1-184.

63. Suryanarayana, C.; Ivanov, E.; Boldyrev, V. The science and technology of mechanical alloying. *Materials Science and Engineering A-Structural Materials Properties Microstructure and Processing* **2001***, 304*, 151-158.

64. Basak, S.; Chen, D.; Biswas, P. Electrospray of ionic precursor solutions to synthesize iron oxide nanoparticles: Modified scaling law. *Chemical Engineering Science* **2007***, 62*, 1263-1268.

65. Morjan, I.; Alexandrescu, R.; Dumitrache, F.; Birjega, R.; Fleaca, C.; Soare, I.; Luculescu, C. R.; Filoti, G.; Kuncer, V.; Vekas, L.; Popa, N. C.; Prodan, G.; Ciupina, V. Iron Oxide-Based Nanoparticles with Different Mean Sizes Obtained by the Laser Pyrolysis: Structural and Magnetic Properties. *Journal of Nanoscience and Nanotechnology* **2010***, 10*, 1223-1234.

66. Popovici, E.; Dumitrache, F.; Morjan, I.; Alexandrescu, R.; Ciupina, V.; Prodan, G.; Vekas, L.; Bica, D.; Marinica, O.; Vasile, E. Iron/iron oxides core-shell nanoparticles by laser pyrolysis: Structural characterization and enhanced particle dispersion. *Appl. Surf. Sci.* **2007***, 254*, 1048-1052.

67. Alexandrescu, R.; Morjan, I.; Voicu, I.; Dumitrache, F.; Albu, L.; Soare, I.; Prodan, G. Combining resonant/non-resonant processes: Nanometer-scale iron-based material preparation via CO2 laser pyrolysis. *Appl. Surf. Sci.* **2005***, 248*, 138-146.

68. Dumitrache, F.; Morjan, I.; Alexandrescu, R.; Ciupina, V.; Prodan, G.; Voicu, I.; Fleaca, C.; Albu, L.; Savoiu, M.; Sandu, I.; Popovici, E.; Soare, I. Iron-iron oxide core-shell nanoparticles synthesized by laser pyrolysis followed by superficial oxidation. *Appl. Surf. Sci.* **2005***, 247*, 25-31.

69. Martelli, S.; Mancini, A.; Giorgi, R.; Alexandrescu, R.; Cojocaru, S.; Crunteanu, A.; Voicu, I.; Balu, M.; Morjan, I. Production of iron-oxide nanoparticles by laser-induced pyrolysis of gaseous precursors. *Appl. Surf. Sci.* **2000***, 154*, 353-359.

70. Gurav, A.; Kodas, T.; Pluym, T.; Xiong, Y. Aerosol Processing of Materials. *Aerosol Science and Technology* **1993***, 19*, 411-452.

71. Albornoz, C.; Jacobo, S. Preparation of a biocompatible magnetic film from an aqueous ferrofluid. *J Magn Magn Mater* **2006***, 305*, 12-15.

72. Kaushika, A.; Khan, R.; Solanki, P. R.; Pandey, P.; Alam, J.; Ahmad, S.; Malhotra, B. D. Iron oxide nanoparticles-chitosan composite based glucose biosensor. *Biosens. Bioelectron.* **2008***, 24*, 676-683.

73. Kim, D.; Zhang, Y.; Voit, W.; Rao, K.; Muhammed, M. Synthesis and characterization of surfactant-coated superparamagnetic monodispersed iron oxide nanoparticles. *J Magn Magn Mater* **2001***, 225*, 30-36.

74. Massart, R.; Cabuil, V. Effect of some Parameters on the Formation of Colloidal Magnetite in Alkaline-Medium - Yield and Particle-Size Control. *J. Chim. Phys. Phys. -Chim. Biol.* **1987***, 84*, 967-973.

75. Lee, J.; Isobe, T.; Senna, M. Preparation of ultrafine Fe3O4 particles by precipitation in the presence of PVA at high pH. *J. Colloid Interface Sci.* **1996***, 177*, 490-494.

76. Massart, R.; Dubois, E.; Cabuil, V.; Hasmonay, E. Preparation and Properties of Monodisperse Magnetic Fluids. *J Magn Magn Mater* **1995***, 149*, 1-5.

77. Sugimoto, T.; Matijevic, E. Formation of Uniform Spherical Magnetite Particles by Crystallization from Ferrous Hydroxide Gels. *J. Colloid Interface Sci.* **1980***, 74*, 227-243.

78. Wan, J.; Chen, X.; Wang, Z.; Yang, X.; Qian, Y. A soft-template-assisted hydrothermal approach to single-crystal Fe3O4 nanorods. *J. Cryst. Growth* **2005***, 276*, 571-576.

79. Chin, A. B.; Yaacob, I. I. Synthesis and characterization of magnetic iron oxide nanoparticles via w/o microemulsion and Massart's procedure. *J. Mater. Process. Technol.* **2007***, 191*, 235-237.

80. Salazar-Alvarez, G.; Muhammed, M.; Zagorodni, A. Novel flow injection synthesis of iron oxide nanoparticles with narrow size distribution. *Chemical Engineering Science* **2006***, 61*, 4625-4633.

81. Lim, B.; Rahtu, A.; Gordon, R. Atomic layer deposition of transition metals. *Nature Materials* **2003***, 2*, 749-754.

82. Teja, A. S.; Koh, P. Synthesis, properties, and applications of magnetic iron oxide nanoparticles. *Progress in Crystal Growth and Characterization of Materials* **2009***, 55*, 22-45.

83. Hyeon, T.; Lee, S.; Park, J.; Chung, Y.; Bin Na, H. Synthesis of highly crystalline and monodisperse maghemite nanocrystallites without a size-selection process. *J. Am. Chem. Soc.* **2001***, 123*, 12798-12801.

84. Zhang, L.; He, R.; Gu, H. Oleic acid coating on the monodisperse magnetite nanoparticles. *Appl. Surf. Sci.* **2006***, 253*, 2611-2617.

85. Kwon, S. G.; Piao, Y.; Park, J.; Angappane, S.; Jo, Y.; Hwang, N.; Park, J.; Hyeon, T. Kinetics of monodisperse iron oxide nanocrystal formation by "heating-up" process. *J. Am. Chem. Soc.* **2007***, 129*, 12571-12584.

86. Roca, A. G.; Morales, M. P.; O'Grady, K.; Serna, C. J. Structural and magnetic properties of uniform magnetite nanoparticles prepared by high temperature decomposition of organic precursors. *Nanotechnology* **2006***, 17*, 2783-2788.

87. Carroll, K. J.; Reveles, J. U.; Shultz, M. D.; Khanna, S. N.; Carpenter, E. E. Preparation of Elemental Cu and Ni Nanoparticles by the Polyol Method: An Experimental and Theoretical Approach. *Journal of Physical Chemistry C* **2011***, 115*, 2656-2664.

88. Miguel-Sancho, N.; Bomati-Miguel, O.; Roca, A. G.; Martinez, G.; Arruebo, M.; Santamaria, J. Synthesis of Magnetic Nanocrystals by Thermal Decomposition in Glycol Media: Effect of Process Variables and Mechanistic Study. *Ind Eng Chem Res* **2012***, 51*, 8348-8357.

89. Fievet, F.; Fievet-Vincent, F.; Lagier, J.; Dumont, B.; Figlarz, M. Controlled Nucleation and Growth of Micrometer-Size Copper Particles Prepared by the Polyol Process. *Journal of Materials Chemistry* **1993***, 3*, 627-632.

90. Kim, E.; Lee, H.; Kwak, B.; Kim, B. Synthesis of ferrofluid with magnetic nanoparticles by sonochemical method for MRI contrast agent. *J Magn Magn Mater* **2005***, 289*, 328-330.

91. Lu, A.; Salabas, E. L.; Schueth, F. Magnetic nanoparticles: Synthesis, protection, functionalization, and application. *Angewandte Chemie-International Edition* **2007***, 46*, 1222-1244.

92. Kharisov, B. I.; Dias, H. V. R.; Kharissova, O. V.; Manuel Jimenez-Perez, V.; Olvera Perez, B.; Munoz Flores, B. Iron-containing nanomaterials: synthesis, properties, and environmental applications. *Rsc Advances* **2012***, 2*, 9325-9358.

93. Hao, R.; Xing, R.; Xu, Z.; Hou, Y.; Gao, S.; Sun, S. Synthesis, Functionalization, and Biomedical Applications of Multifunctional Magnetic Nanoparticles. *Adv Mater* **2010***, 22*, 2729-2742.

94. Sato, S.; Murakata, T.; Yanagi, H.; Miyasaka, F.; Iwaya, S. Hydrothermal Synthesis of Fine Perovskite Pbtio3 Powders with a Simple Mode of Size Distribution. *J. Mater. Sci.* **1994***, 29*, 5657-5663.

95. Sun, S.; Zeng, H.; Robinson, D.; Raoux, S.; Rice, P.; Wang, S.; Li, G. Monodisperse MFe2O4 (M = Fe, Co, Mn) nanoparticles. *J. Am. Chem. Soc.* **2004***, 126*, 273-279.

96. Liong, M.; Shao, H.; Haun, J. B.; Lee, H.; Weissleder, R. Carboxymethylated Polyvinyl Alcohol Stabilizes Doped Ferrofluids for Biological Applications. *Adv Mater* **2010***, 22*, 5168-+.

97. Qiao, R.; Yang, C.; Gao, M. Superparamagnetic iron oxide nanoparticles: from preparations to in vivo MRI applications. *Journal of Materials Chemistry* **2009***, 19*, 6274-6293.

98. Cosmetic Ingredient Review Expert Final report on the safety assessment of Benzyl Alcohol, Benzoic Acid, and Sodium Benzoate. *Int. J. Toxicol.* **2001***, 20*, 23-50.

99. Scognamiglio, J.; Jones, L.; Vitale, D.; Letizia, C. S.; Api, A. M. Fragrance material review on benzyl alcohol. *Food and Chemical Toxicology* **2012***, 50*, S140-S160.

100. Belsito, D.; Bickers, D.; Bruze, M.; Calow, P.; Dagli, M. L.; Fryer, A. D.; Greim, H.; Miyachi, Y.; Saurath, J. H.; Sipes, I. G.; RIFM Expert Panel A toxicological and dermatological assessment of aryl alkyl alcohols when used as fragrance ingredients. *Food and Chemical Toxicology* **2012***, 50*, S52-S99.

101. Sudareva, N.; Chubarova, E. Time-dependent conversion of benzyl alcohol to benzaldehyde and benzoic acid in aqueous solutions. *J. Pharm. Biomed. Anal.* **2006***, 41*, 1380-1385.

102. Niederberger, M.; Bartl, M.; Stucky, G. Benzyl alcohol and titanium tetrachloride - A versatile reaction system for the nonaqueous and low-temperature preparation of crystalline and luminescent titania nanoparticles. *Chemistry of Materials* **2002***, 14*, 4364-4370.

103. Niederberger, M.; Bartl, M. H.; Stucky, G. D. Benzyl Alcohol and Transition Metal Chlorides as a Versatile Reaction System for the Nonaqueous and Low-Temperature Synthesis of Crystalline Nano-Objects with Controlled Dimensionality. *J. Am. Chem. Soc.* **2002***, 124*, 13642-13643.

104. Pinna, N.; Niederberger, M. Surfactant-free nonaqueous synthesis of metal oxide nanostructures. *Angewandte Chemie-International Edition* **2008***, 47*, 5292-5304.

105. Bilecka, I.; Djerdj, I.; Niederberger, M. One-minute synthesis of crystalline binary and ternary metal oxide nanoparticles. *Chemical Communications* **2008**, 886-888.

106. Garnweitner, G.; Niederberger, M. Nonaqueous and Surfactant-Free Synthesis Routes to Metal Oxide Nanoparticles. *J Am Ceram Soc* **2006***, 89*, 1801-1808.

107. Garnweitner, G.; Goldenberg, L.; Sakhno, O.; Antonietti, M.; Niederberger, M.; Stumpe, J. Large-Scale Synthesis of Organophilic Zirconia Nanoparticles and their Application in Organic?Inorganic Nanocomposites for Efficient Volume Holography. *Small* **2007***, 3*, 1626-1632.

108. Zhou, S.; Garnweitner, G.; Niederberger, M.; Antonietti, M. Dispersion Behavior of Zirconia Nanocrystals and Their Surface Functionalization with Vinyl Group-Containing Ligands. *Langmuir* **2007***, 23*, 9178-9187.

109. Pinna, N.; Grancharov, S.; Beato, P.; Bonville, P.; Antonietti, M.; Niederberger, M. Magnetite nanocrystals: Nonaqueous synthesis, characterization, and solubility. *Chemistry of Materials* **2005***, 17*, 3044-3049.

110. Tartaj, P.; Morales, M. P.; Gonzalez-carreño, T.; Veintemillas-verdaguer, S.; Serna, C. J. The Iron Oxides Strike Back: From Biomedical Applications to Energy Storage Devices and Photoelectrochemical Water Splitting. *Adv Mater* **2011***, 23*, 5243-5249.

111. Haberl, J. M.; Sanchez-Ferrer, A.; Mihut, A. M.; Dietsch, H.; Hirt, A. M.; Mezzenga, R. Liquid-Crystalline Elastomer-Nanoparticle Hybrids with Reversible Switch of Magnetic Memory. *Adv Mater* **2013***, 25*, 1787-1791.

112. Batlle, X.; Labarta, A. Finite-size effects in fine particles: magnetic and transport properties. *Journal of Physics D-Applied Physics* **2002***, 35*, R15-R42.

113. LesliePelecky, D.; Rieke, R. Magnetic properties of nanostructured materials. *Chemistry of Materials* **1996***, 8*, 1770-1783.

114. Taylor, R.; Coulombe, S.; Otanicar, T.; Phelan, P.; Gunawan, A.; Lv, W.; Rosengarten, G.; Prasher, R.; Tyagi, H. Small particles, big impacts: A review of the diverse applications of nanofluids. *J. Appl. Phys.* **2013***, 113*, 011301.

115. Li, L.; Leung, C. W.; Pong, P. W. T. Magnetism of Iron Oxide Nanoparticles and Magnetic Biodetection. *Journal of Nanoelectronics and Optoelectronics* **2013***, 8*, 397-414.

116. Li, L.; Mak, K. Y.; Leung, C. W.; Ng, S. M.; Lei, Z. Q.; Pong, P. W. T. Detection of 10-nm Superparamagnetic Iron Oxide Nanoparticles Using Exchange-Biased GMR Sensors in Wheatstone Bridge. *IEEE Trans. Magn.* **2013***, 49*, 4056-4059.

117. Wang, J.; Zhu, Z.; Munir, A.; Zhou, H. S. Fe(3)O(4) nanoparticles-enhanced SPR sensing for ultrasensitive sandwich bio-assay. *Talanta* **2011***, 84*, 783-788.

118. Blanc-Beguin, F.; Nabily, S.; Gieraltowski, J.; Turzo, A.; Querellou, S.; Salaun, P. Y. Cytotoxicity and GMI bio-sensor detection of maghemite nanoparticles internalized into cells. *J Magn Magn Mater* **2009***, 321*, 192-197.

119. Lu, A.; Salabas, E. L.; Schueth, F. Magnetic nanoparticles: Synthesis, protection, functionalization, and application. *Angewandte Chemie-International Edition* **2007***, 46*, 1222-1244.

120. Polshettiwar, V.; Luque, R.; Fihri, A.; Zhu, H.; Bouhrara, M.; Bassett, J. Magnetically Recoverable Nanocatalysts. *Chem. Rev.* **2011***, 111*, 3036-3075.

121. Yang, H.; Zhang, S.; Chen, X.; Zhuang, Z.; Xu, J.; Wang, X. Magnetite-containing spherical silica nanoparticles for biocatalysis and bioseparations. *Anal. Chem.* **2004***, 76*, 1316-1321.

122. Yi, D. K.; Lee, S. S.; Ying, J. Y. Synthesis and applications of magnetic nanocomposite catalysts. *Chemistry of Materials* **2006***, 18*, 2459-2461.

123. Frey, N. A.; Peng, S.; Cheng, K.; Sun, S. Magnetic nanoparticles: synthesis, functionalization, and applications in bioimaging and magnetic energy storage. *Chem. Soc. Rev.* **2009***, 38*, 2532-2542.

124. Coffey, W. T.; Kalmykov, Y. P. Thermal fluctuations of magnetic nanoparticles: Fifty years after Brown. *J. Appl. Phys.* **2012***, 112*, 121301.

125. Wabler, M.; Zhu, W.; Hedayati, M.; Attaluri, A.; Zhou, H.; Mihalic, J.; Geyh, A.; DeWeese, T. L.; Ivkov, R.; Artemov, D. Magnetic resonance imaging contrast of iron oxide nanoparticles developed for hyperthermia is dominated by iron content. *International Journal of Hyperthermia* **2014***, 30*, 192-200.

126. Park, J. Y.; Choi, H. J.; Nam, G.; Cho, K.; Son, J. In Vivo Dual-Modality Terahertz/Magnetic Resonance Imaging Using Superparamagnetic Iron Oxide Nanoparticles as a Dual Contrast Agent. *Ieee Transactions on Terahertz Science and Technology* **2012***, 2*, 93-98.

127. Boutry, S.; Brunin, S.; Mahieu, I.; Laurent, S.; Elst, L. V.; Muller, R. N. Magnetic labeling of non-phagocytic adherent cells with iron oxide nanoparticles: a comprehensive study. *Contrast Media & Molecular Imaging* **2008***, 3*, 223-232.

128. Chapon, C.; Franconi, F.; Lemaire, L.; Marescaux, L.; Legras, P.; Saint-Andre, J.; Denizot, B.; Le Jeune, J. High field magnetic resonance imaging evaluation of superparamagnetic iron oxide nanoparticles in a permanent rat myocardial infarction. *Invest. Radiol.* **2003***, 38*, 141-146.

129. Ishigami, K.; Tajima, T.; Fujita, N.; Nishie, A.; Asayama, Y.; Kakihara, D.; Nakayama, T.; Okamoto, D.; Taketomi, A.; Shirabe, K.; Honda, H. Hepatocellular

carcinoma with marginal superparamagnetic iron oxide uptake on T2*-weighted magnetic resonance imaging: Histopathologic correlation. *Eur. J. Radiol.* **2011***, 80*, E293-E298.

130. Vallejo-Fernandez, G.; O'Grady, K. Effect of the distribution of anisotropy constants on hysteresis losses for magnetic hyperthermia applications. *Appl. Phys. Lett.* **2013***, 103*, 142417.

131. Simeonidis, K.; Martinez-Boubeta, C.; Balcells, L.; Monty, C.; Stavropoulos, G.; Mitrakas, M.; Matsakidou, A.; Vourlias, G.; Angelakeris, M. Fe-based nanoparticles as tunable magnetic particle hyperthermia agents. *J. Appl. Phys.* **2013***, 114*, 103904.

132. Neuberger, T.; Schopf, B.; Hofmann, H.; Hofmann, M.; von Rechenberg, B. Superparamagnetic nanoparticles for biomedical applications: Possibilities and limitations of a new drug delivery system. *J Magn Magn Mater* **2005***, 293*, 483-496.

133. Weiss, W.; Ranke, W. Surface chemistry and catalysis on well-defined epitaxial iron-oxide layers. *Prog Surf Sci* **2002***, 70*, 1-151.

134. Li, X.; Elliott, D. W.; Zhang, W. Zero-valent iron nanoparticles for abatement of environmental pollutants: Materials and engineering aspects. *Critical Reviews in Solid State and Materials Sciences* **2006***, 31*, 111-122.

135. Cornell, R. M.; Schwertmann, U. *The Iron Oxides: Structure, Properties, Reactions, Occurences and Uses, Second Edition;* Wiley-VCH: Weinhiem, 2004; .

136. Zhang, Z.; Satpathy, S. Electron-States, Magnetism, and the Verwey Transition in Magnetite. *Physical Review B* **1991***, 44*, 13319-13331.

137. Walz, F. The Verwey transition - a topical review. *Journal of Physics-Condensed Matter* **2002***, 14*, R285-R340.

138. Weiss, W.; Ranke, W. Surface chemistry and catalysis on well-defined epitaxial iron-oxide layers. *Prog Surf Sci* **2002***, 70*, 1-151.

139. Ketteler, G.; Weiss, W.; Ranke, W.; Schlogl, R. Bulk and surface phases of iron oxides in an oxygen and water atmosphere at low pressure. *Physical Chemistry Chemical Physics* **2001***, 3*, 1114-1122.

140. Cornell, R. M. *The iron oxides : structure, properties, reactions, occurrences, and uses;* Weinheim : Wiley-VCH: Weinheim, 2003; .

141. Zboril, R.; Mashlan, M.; Petridis, D. Iron(III) oxides from thermal processes-synthesis, structural and magnetic properties, Mossbauer spectroscopy characterization, and applications. *Chemistry of Materials* **2002***, 14*, 969-982.

142. Makie, P.; Westin, G.; Persson, P.; Osterlund, L. Adsorption of Trimethyl Phosphate on Maghemite, Hematite, and Goethite Nanoparticles. *Journal of Physical Chemistry a* **2011***, 115*, 8948-8959.

143. Darken, L. S.; Gurry, R. W. The System Iron-Oxygen. I. The WÃ¼stite Field and Related Equilibria. *J. Am. Chem. Soc.* **1945***, 67*, 1398-1412.

144. Pankhurst, Q.; Connolly, J.; Jones, S.; Dobson, J. Applications of magnetic nanoparticles in biomedicine. *Journal of Physics D-Applied Physics* **2003***, 36*, R167-R181.

145. Baumgartner, J.; Bertinetti, L.; Widdrat, M.; Hirt, A. M.; Faivre, D. Formation of Magnetite Nanoparticles at Low Temperature: From Superparamagnetic to Stable Single Domain Particles. *Plos One* **2013***, 8*, e57070.

146. Butler, R.; Banerjee, S. Theoretical Single-Domain Grain-Size Range in Magnetite and Titanomagnetite. *Journal of Geophysical Research* **1975***, 80*, 4049-4058.

147. Langford, J.; Louer, D. Powder diffraction. *Reports on Progress in Physics* **1996***, 59*, 131-234.

148. Harris, K.; Tremayne, M. Crystal structure determination from powder diffraction data. *Chemistry of Materials* **1996***, 8*, 2554-2570.

149. Vickerman, J.; Gilmore, I. *Surface analysis the principal techniques;* Chichester, U.K. : Wiley: Chichester, U.K., 2009; .

150. Kasap, S. O. (. *Principles of electronic materials and devices;* Boston : McGraw-Hill: Boston, 2006; .

151. Lin, P.; Lin, S.; Wang, P. C.; Sridhar, R. Techniques for physicochemical characterization of nanomaterials. *Biotechnol. Adv.* **2014***, 32*, 711-726.

152. Lim, J.; Yeap, S. P.; Che, H. X.; Low, S. C. Characterization of magnetic nanoparticle by dynamic light scattering. *Nanoscale Research Letters* **2013***, 8*, 381.

153. Hiemenz, P. C., 1936- *Principles of colloid and surface chemistry;* New York : Marcel Dekker: New York, 1997; .

154. Wang, Z. Transmission electron microscopy of shape-controlled nanocrystals and their assemblies. *J Phys Chem B* **2000***, 104*, 1153-1175.

155. Zhang, Z.; Miao, C.; Guo, W. Nano-solenoid: helicoid carbon-boron nitride hetero-nanotube. *Nanoscale* **2013***, 5*, 11902-11909.

156. Sun, S.; Zeng, H. Size-controlled synthesis of magnetite nanoparticles. *J. Am. Chem. Soc.* **2002***, 124*, 8204-8205.

157. Florini, N.; Barrera, G.; Tiberto, P.; Allia, P.; Bondioli, F. Nonaqueous Sol-Gel Synthesis of Magnetic Iron Oxides Nanocrystals. *J Am Ceram Soc* **2013***, 96*, 3169-3175.

158. Tu, Z.; Zhang, B.; Yang, G.; Wang, M.; Zhao, F.; Sheng, D.; Wang, J. Synthesis of poly(ethylene glycol) and poly(vinyl pyrrolidone) co-coated superparamagnetic iron oxide nanoparticle as a pH-sensitive release drug carrier. *Colloids and Surfaces A-Physicochemical and Engineering Aspects* **2013***, 436*, 854-861.

159. Yu, W.; Falkner, J.; Yavuz, C.; Colvin, V. Synthesis of monodisperse iron oxide nanocrystals by thermal decomposition of iron carboxylate salts. *Chemical Communications* **2004**, 2306-2307.

160. Sangermano, M.; Allia, P.; Tiberto, P.; Barrera, G.; Bondioli, F.; Florini, N.; Messori, M. Photo-Cured Epoxy Networks Functionalized With Fe3O4 Generated by Non-hydrolytic SolGel Process. *Macromolecular Chemistry and Physics* **2013***, 214*, 508-516.

161. Fievet, F.; Lagier, J.; Blin, B.; Beaudoin, B.; Figlarz, M. Homogeneous and Heterogeneous Nucleations in the Polyol Process for the Preparation of Micron and Sub-Micron Size Metal Particles. *Solid State Ionics* **1989***, 32-3*, 198-205.

162. Katritzky, A.; Mu, L.; Lobanov, V.; Karelson, M. Correlation of boiling points with molecular structure .1. A training set of 298 diverse organics and a test set of 9 simple inorganics. *J. Phys. Chem.* **1996***, 100*, 10400-10407.

163. Nandwana, V.; Elkins, K.; Liu, J. Magnetic hardening in ultrafine FePt nanoparticle assembled films. *Nanotechnology* **2005***, 16*, 2823-2826.

164. Goss, C. Saturation Magnetization, Coercivity and Lattice-Parameter Changes in the System Fe3o4-Gamma-Fe2o3, and their Relationship to Structure. *Physics and Chemistry of Minerals* **1988***, 16*, 164-171.

165. Shultz, M. D.; Braxton, W.; Taylor, C.; Carpenter, E. E. One parameter control of the size of iron oxide nanoparticles synthesized in reverse micelles. *J. Appl. Phys.* **2009***, 105*, 07A522.

166. LaMer, V. K.; Dinegar, R. H. Theory, Production and Mechanism of Formation of Monodispersed Hydrosols. *J. Am. Chem. Soc.* **1950***, 72*, 4847-4854.

167. Wang, H.; Nann, T. Monodisperse Upconverting Nanocrystals by Microwave-Assisted Synthesis. *Acs Nano* **2009***, 3*, 3804-3808.

168. Finney, E. E.; Finke, R. G. Nanocluster nucleation and growth kinetic and mechanistic studies: A review emphasizing transition-metal nanoclusters. *J. Colloid Interface Sci.* **2008***, 317*, 351-374.

169. Rao, C. N. R.; Müller, A.; Cheetham, A. K. *Nanomaterials chemistry : recent developments and new directions;* Weinheim : Wiley-VCH ; Chichester : John Wiley, distributor: Weinheim : Chichester, 2007; .

170. Figuerola, A.; Fiore, A.; Di Corato, R.; Falqui, A.; Giannini, C.; Micotti, E.; Lascialfari, A.; Corti, M.; Cingolani, R.; Pellegrino, T.; Cozzoli, P. D.; Manna, L. One-pot synthesis and characterization of size-controlled bimagnetic FePt-iron oxide heterodimer nanocrystals. *J. Am. Chem. Soc.* **2008***, 130*, 1477-1487.

171. Tao, A. R.; Habas, S.; Yang, P. Shape control of colloidal metal nanocrystals. *Small* **2008***, 4*, 310-325.

172. Murray, C.; Norris, D.; Bawendi, M. Synthesis and Characterization of nearly Monodisperse Cde (E = S, Se, Te) Semiconductor Nanocrystallites. *J. Am. Chem. Soc.* **1993***, 115*, 8706-8715.

173. Symposium on Particle Growth in Suspensions (1972,: Brunel University *Particle growth in suspensions; proceedings;* London, New York, Academic Press: London, New York, 1973; .

174. Reiss, H. The Growth of Uniform Colloidal Dispersions. *J. Chem. Phys.* **1951***, 19*, 482-487.

175. Chen, Y.; Johnson, E.; Peng, X. Formation of monodisperse and shape-controlled MnO nanocrystals in non-injection synthesis: Self-focusing via. *J. Am. Chem. Soc.* **2007***, 129*, 10937-10947.

176. Huang, J.; Parab, H. J.; Liu, R.; Lai, T.; Hsiao, M.; Chen, C.; Sheu, H.; Chen, J.; Tsai, D.; Hwu, Y. Investigation of the growth mechanism of iron oxide nanoparticles via a seed-mediated method and its cytotoxicity studies. *Journal of Physical Chemistry C* **2008***, 112*, 15684-15690.

Vita

Stanley Eugene Gilliland III was born on June 16, 1989 in Nashville, Tennessee and is an American Citizen. He is a member of the Seneca-Cayuga Tribe of Oklahoma. In 2007, he graduated from Bluestone Senior High School in Skipwith, Virginia. After high school, he attended James Madison University in Harrisonburg, Virginia where he received his Bachelor of Science in Biotechnology in December of 2010.

Submitted Peer-reviewed Research Paper:

i. Gilliland, S. E.; Carpenter, E. E., Shultz, M. D. Modified Seed Growth of Iron Oxide Nanoparticles in Benzyl Alcohol: Optimized Synthesis and Surface Functionalization for Heating and Broad Stability in Biomedical Applications. *Nanobiomedicine.* 2014. Ref.: Ms. No. NBM.2014.00010R1.